

## Retention of water in terrestrial magma oceans and carbon-rich early atmospheres

DAN J. BOWER <sup>1</sup>, KAUSTUBH HAKIM <sup>1</sup>, PAOLO A. SOSSI <sup>2</sup>, AND PATRICK SANAN <sup>3</sup>

<sup>1</sup>*Center for Space and Habitability, University of Bern  
Gesellschaftsstrasse 6  
3012 Bern, Switzerland*

<sup>2</sup>*Institute of Geochemistry and Petrology, Department of Earth Sciences, ETH Zurich  
Clausiusstrasse 25  
8092 Zurich, Switzerland*

<sup>3</sup>*Institute of Geophysics, ETH Zurich  
Sonneggstrasse 5  
8092 Zurich, Switzerland*

(Received July 14, 2021; Revised October 12, 2021; Accepted TBD)

Submitted to The Planetary Science Journal

### ABSTRACT

Massive steam and CO<sub>2</sub> atmospheres have been proposed for magma ocean outgassing of Earth and terrestrial planets. Yet formation of such atmospheres depends on volatile exchange with the molten interior, governed by volatile solubilities and redox reactions. We determine the evolution of magma ocean–atmosphere systems for a range of oxygen fugacity, C/H ratio and hydrogen budget that include redox reactions for hydrogen (H<sub>2</sub>–H<sub>2</sub>O), carbon (CO–CO<sub>2</sub>), methane (CH<sub>4</sub>), and solubility laws for H<sub>2</sub>O and CO<sub>2</sub> for silicate melts. We find that small initial budgets of hydrogen, high C/H ratios, and oxidising conditions, suppress outgassing of hydrogen until the late stages of magma ocean crystallisation. Hence early atmospheres in equilibrium with magma oceans are dominantly carbon-rich, and specifically CO-rich except at the most oxidising conditions. The high solubility of H<sub>2</sub>O limits its outgassing to melt fractions below ~30%; the fraction at which the mantle transitions from vigorous-to sluggish convection with melt percolation. Inefficient melt percolation may prevent further crystallisation before a surface lid forms, which can delay or prevent most water (>75%) from outgassing, thereby hindering the formation of surface oceans. Alternatively, with efficient melt percolation or mechanism to break the lid, a molten surface could be maintained, enabling the transition from a CO-rich to water-rich atmosphere during the late stage of crystallisation. We conclude that a large fraction of the water delivered to terrestrial planets over their accretion histories may be safely harboured in their interiors during the magma ocean phase and outgas only gradually over geological timescales.

*Keywords:* Planetary interior — Planetary atmospheres — Planetary structure — Super Earths — Extrasolar rocky planets — Exoplanet atmospheric composition — Exoplanet evolution

### 1. INTRODUCTION

The origin and distribution of light volatile elements such as C, H and O, in the major planetary reservoirs (core, mantle, and atmosphere) regulates how terres-

trial planet atmospheres form and evolve (Gaillard et al. 2021, and references therein). During planetary accretion and contemporaneous iron-core formation—both of which promote the formation of a global magma ocean—the siderophile nature of both C (Corgne et al. 2008) and H (Tagawa et al. 2021) strongly partitions them into the core. The fractions of these volatile elements that partition into the core are regulated by their solubilities in silicate liquid, set at the magma ocean–atmosphere in-

terface. Hence, the mantle retains some fraction of C at core forming conditions, in addition to replenishment of both C and H post-core formation (Hirschmann 2016), which subsequently participates in short- and long-term geochemical cycling (e.g., Dasgupta 2013). Here we examine how the inventories of C and H exchange between the interior and atmosphere as the magma ocean evolves post-core formation.

The magma ocean outgasses volatiles as it cools from molten to mostly solid silicate rock to form a secondary atmosphere. Therefore, chemical and physical processes operating in the magma ocean, both at its surface and at depth, exert strong controls on the size and composition of such early atmospheres. Early atmospheres establish the initial conditions for the subsequent long-term evolution of planetary interiors and their atmospheres through interaction with the surface environment via geochemical cycles. Therefore, they connect processes occurring during and soon after planet and iron-rich core formation to the establishment of long-term climate states.

The shock degassing of substantial H<sub>2</sub>O from hydrated minerals (Lange & Ahrens 1982) to simulate impacts during planetary accretion motivated investigation of the blanketing effect of a steam atmosphere above the molten early Earth (Abe & Matsui 1985). Additional justification for the widespread presence of H<sub>2</sub>O and CO<sub>2</sub> is provided by experiments and accompanying equilibrium models for the devolatilisation of ordinary and carbonaceous chondrites, which are shown to produce oxidised species in abundance (Gooding & Muenow 1977; Schaefer & Fegley 2010; Thompson et al. 2021). Consequently, coupled magma ocean–atmosphere models have focused almost exclusively on the role of oxidised species (H<sub>2</sub>O and CO<sub>2</sub>) in controlling the lifetime of magma oceans and growth of early atmospheres (e.g., Lebrun et al. 2013; Salvador et al. 2017; Nikolaou et al. 2019; Barth et al. 2021).

More reduced materials (such as enstatite chondrites that are thought to have contributed to Earth’s accretion on isotopic grounds) may instead produce H<sub>2</sub>-rich or CO-rich gases (Schaefer & Fegley 2010). This has partly inspired calculations of the chemistry and cooling timescales of reducing atmospheres (Zahnle et al. 2020; Lichtenberg et al. 2021). However, chondrites may not be appropriate analogues for the materials that degas to produce early atmospheres around terrestrial planets (Sossi 2021). This is because mass transfer is much more efficient when materials are liquid rather than solid, allowing for the more rapid replenishment of surface material via convection and thus facilitating atmosphere formation. This has further led coupled models to un-

derstand the astrophysical observables of magma oceans to interpret the spectroscopic data from next generation telescopes (Hamano et al. 2015; Bonati et al. 2019; Bower et al. 2019; Katyal et al. 2020).

The redox state (more precisely, the oxygen fugacity,  $f_{\text{O}_2}$ ) of the mantle depends on pressure, temperature, and composition, and dictates the speciation of outgassing products. It controls the relative fugacities of reduced and oxidised species, which is equivalent to partial pressure at the low total pressures of terrestrial atmospheres. Core formation on Earth established  $f_{\text{O}_2}$  around two log<sub>10</sub> units below the iron-wüstite buffer (IW) at equilibrium at depth, based on the Fe content of the mantle and core (e.g., Rubie et al. 2015). However, the volume change of the reaction between ferric and ferrous iron means that silicate melt transported to the surface defines higher  $f_{\text{O}_2}$  than that set by core formation (Armstrong et al. 2019; Hirschmann 2012). The surface  $f_{\text{O}_2}$ , rather than the  $f_{\text{O}_2}$  at depth, imposes the redox state at the magma ocean–atmosphere interface and thereby controls outgassing chemistry (Sossi et al. 2020).

Evolutionary models of magma oceans are usually derived from geochemical or geodynamic considerations. Chemical models focus on tracking the compositional evolution of cumulate mineral assemblages which form as the magma ocean cools (e.g., Elkins-Tanton 2008). However, they ignore dynamics during the crystallisation process and often assume fractional crystallisation. In (stepwise) fractional crystallisation, cumulates that form due to cooling are isolated from the molten magma ocean and the evolving composition of the melt is determined from mass balance. By contrast, dynamic models track thermal energy transport but at the expense of reduced compositional complexity. However, dynamic formulations that include a local representation of melt–solid separation (Abe 1993; Bower et al. 2018) can replicate fractional crystallisation. They can also replicate equilibrium crystallisation, in which melt and solid freezes together before any significant relative motion has occurred.

Hence in this study we exploit a dynamical model to probe the relationship between crystallisation style—fractional or equilibrium crystallisation—and its consequence for early atmosphere formation. To this end, we combine mass balance and equilibrium chemistry in a self-consistent and time-evolved model to probe magma ocean–atmosphere exchange. This takes into account the CO<sub>2</sub>/CO, H<sub>2</sub>O/H<sub>2</sub>, and CH<sub>4</sub>/CO<sub>2</sub> ratios set by the oxygen fugacity, C/H ratio and temperature of the magma ocean, and their relative solubilities. We explore a range of initial endowments of the hydrogen and

carbon volatile inventory, and quantify the relationship between these variables and the partial pressures of the degassed species. Finally, atmospheric escape is also modelled to determine the extent to which the preferential loss of hydrogen can influence the subsequent outgassing of dissolved volatiles.

## 2. INTERIOR-ATMOSPHERE COUPLING

### 2.1. Overview

The SPIDER code (Bower et al. 2018, 2019) solves for the coupled evolution of the silicate mantle and atmosphere, where the mantle can be molten, solid, or a mixture (partial melt). It considers interior energy transport by convection, conduction, and relative motion of melt and solid through mixing and separation and is a true 1-D model in the sense that energy fluxes are determined locally (Abe 1993; Bower et al. 2018). Cooling of the interior is regulated by radiative transfer in the atmosphere, and the atmosphere itself grows through outgassing of the interior as the mantle solidifies due to cooling. We consider a two phase system of single composition ( $\text{MgSiO}_3$ ), where the thermophysical properties of solid and melt are determined from Mosenfelder et al. (2009) and Wolf & Bower (2018), respectively. The melting curves adhere to peridotite melting data in the upper mantle and measurements on chondritic material in the lower mantle (Andraut et al. 2011); they are not perturbed according to the mantle volatile content. The atmosphere is treated as grey with no scattering and the two-stream approximation is applied to solve for radiative transfer (Abe & Matsui 1985). Opacities of the gas species are provided in Appendix A.

We modified the SPIDER code to additionally account for mass exchange between volatiles according to equilibrium chemistry (Section 2.3) as well as atmospheric escape (Section 2.4). The mathematical description of the volatile mass balance and its adherence to equilibrium chemistry is described in detail in Appendix C. For each chemical reaction, we introduce a term into the volatile mass balance to account for the exchange of mass necessary to retain chemical equilibrium between participating gas species as dictated by oxygen fugacity and temperature. Similarly, another term in the mass balance equation tracks volatile loss due to atmospheric escape. Hence, chemical equilibrium and escape are self-consistently determined as part of the same system of equations that are integrated to describe the coupled interior-atmosphere evolution.

Our parameter choices are similar to those in Bower et al. (2018, 2019) so we only present pertinent details here. We consider a planet at 1 AU with Earth dimensions and a magma ocean that crystallises from the

bottom-up, an approach that is justified owing to the steeper melting curves compared to the mantle adiabat. Convection and melt-solid mixing is determined by an eddy diffusivity which is based on a constant mixing length, and internal heat sources are not considered because their influence is negligible over the lifetime of a magma ocean. Viscosity controls the dynamic regime of the mantle and varies from  $10^2$  Pa s for pure silicate melt to  $10^{22}$  Pa s for pure solid, increasingly abruptly at a melt fraction of 40% (Costa et al. 2009; Bower et al. 2018). Other controls on viscosity, such as temperature and composition, are second order and therefore neglected. The crystal size, which controls the efficiency of melt-solid separation, is set at either 1 mm or 5 cm (Appendix B) to simulate equilibrium or fractional crystallisation, respectively.

We track the reservoir evolution of five volatile species during the magma ocean stage:  $\text{H}_2$ ,  $\text{H}_2\text{O}$ ,  $\text{CO}$ ,  $\text{CO}_2$ , and  $\text{CH}_4$ . For convenience, we refer to  $\text{H}_2\text{O}$  and  $\text{H}_2$  as hydrogen species, and  $\text{CO}$ ,  $\text{CO}_2$ , and  $\text{CH}_4$  as carbon species. The dissolved content of  $\text{H}_2\text{O}$  and  $\text{CO}_2$  in the magma ocean is determined by their solubility, and reduced species are set to zero solubility (Section 2.2). Redox reactions impose  $\text{H}_2$ - $\text{H}_2\text{O}$ ,  $\text{CO}$ - $\text{CO}_2$ , and  $\text{CO}_2$ - $\text{H}_2$ - $\text{CH}_4$  equilibrium (Section 2.3). Partitioning of volatiles into solids (crystals) is not considered because its effect is small compared to the partitioning of volatiles between the melt and atmosphere. Therefore, the amount of volatiles stored in the mantle during solidification is a minimum estimate. We simulate cooling of a magma ocean from an initial surface temperature of 2700 K until it reaches 1650 K. For surface temperatures cooler than 1650 K the assumption of equilibrium dissolution begins to break down. This is because a rheological transition caused by increasing crystal fraction results in mass transfer that is too sluggish to maintain equilibrium with the atmosphere; for conciseness we subsequently refer to this event as ‘surface lid formation’.

### 2.2. Solubility

A solubility law relates the dissolved volatile content of a particular species in melt  $X$  to its fugacity  $f$ . The majority of experimental studies on the solubilities of H and C have been performed at high pressures (few GPa), in order to constrain their degassing during magma genesis—for example at mid-ocean ridges or subduction zones on modern Earth—or alternatively during core formation in a shallow magma ocean. By contrast, pressures at the magma ocean-atmosphere interface of an Earth-sized planet are expected to be around two orders of magnitude less; namely, several hundred bar. This motivates our subsequent choice of solubility laws.

### 2.2.1. Solubility of $H_2O$

We employ a general expression for solubility with a power law dependence:

$$X = \alpha f^{1/\beta}, \quad (1)$$

where  $\alpha$  and  $\beta$  are constants specific to a particular equilibrium between a gas species and its dissolved component. In Equation 1,  $\alpha$  is an empirically-determined coefficient that encompasses the temperature, pressure and composition of the liquid in which the solubility is being determined, while  $\beta$  reflects the stoichiometric relationship between the mole fraction of the dissolved species and the fugacity of the gas species. Henry's law is recovered when  $\beta = 1$ , which indicates no chemical reaction (hence no change in speciation) when the gas dissolves in the solvent. Throughout this work we assume gas ideality such that fugacity and partial pressure are equivalent and hence symbols for fugacity  $f$  and partial pressure  $p$  are used interchangeably. In Equation 1, the relevant partial pressure (fugacity) is determined at the interface of the magma ocean and atmosphere.

At low  $H_2O$  fugacities, water dissolves in silicate melts as hydroxyl ( $OH^-$ ) group so  $\beta_{H_2O} = 2$  describes the solubility of  $H_2O$  in melt (e.g., [McMillan 1994](#)). However, this relationship breaks down at high  $H_2O$  fugacities because  $H_2O$  replaces  $OH^-$  as the predominant melt species (above  $\sim 2000$  bar, [Berndt et al. 2002](#); [Stolper 1982](#)). Therefore, a single  $\beta_{H_2O}$  determined by simply best-fitting data across large  $fH_2O$  ranges yields spurious values of  $\beta_{H_2O}$  because different reactions govern solubility at different  $fH_2O$ .

Table 1 summarises recent experimental constraints on  $H_2O$  solubility for compositions, pressures, and temperatures relevant to the magma ocean–atmosphere interface of a terrestrial planet, i.e. a few hundred bars and greater than about 1500 K. The table is ordered based on the silica content of the sample, increasing from less than 45 wt%  $SiO_2$  to more than 50 wt%  $SiO_2$ . Experiments on evolved compositions (e.g. rhyolitic/granitic melts) are not included because they are not representative of compositions during the magma ocean stage: these are instead summarised in [Iacono-Marziano et al. \(2012\)](#).

Peridotite is a rock comprised predominantly of olivine, which is the major constituent of Earth's mantle and likely exoplanetary mantles ([Putirka & Rarick 2019](#)). The solubility of water in liquid peridotite (red line, Figure 1) is determined at high temperature and low  $fH_2O$ , so its solubility law is most appropriate for a terrestrial magma ocean ([Sossi et al. 2021](#)). For the relevant pressure–temperature conditions of the magma ocean surface, the mole fraction of  $H_2O$  dissolved de-

pends largely on variations in  $fH_2O$ , while the effect of temperature is a subordinate ([Hamilton & Oxtoby 1986](#)), if not poorly constrained variable. As such, temperature does not explicitly appear as a functional dependence in Equation 1 and  $\alpha$  is taken to be constant.

### 2.2.2. Solubility of $CO_2$

There are no experimental constraints on the solubility of  $CO_2$  in primitive mantle compositions, so instead we necessarily use a solubility law formulated for basalt as a proxy. At low  $CO_2$  fugacities, carbon dioxide dissolves in silicate melts as either molecular  $CO_2$  or as the  $CO_3^{2-}$  group ([Stolper & Holloway 1988](#)). Because the stability of the carbonate ion increases according to melt basicity ( $Mg^{2+}$ ,  $Ca^{2+}$  cations, [Holloway & Blank \(1994\)](#)), the Mg-rich nature of planetary mantles ensures that it occurs exclusively as  $CO_3^{2-}$  in such liquids. Determining the mole fraction of dissolved carbonate for pressures up to 815 bar  $fCO_2$ , [Dixon et al. \(1995\)](#) constrained the solubility of  $CO_2$  in Mid-Ocean Ridge Basalt (MORB) melt:

$$X_{CO_2}^m = (3.8 \times 10^{-7}) fCO_2 \exp\left(-23 \frac{fCO_2 - 1}{10RT}\right), \quad (2)$$

where  $X_{CO_2}^m$  is the mole fraction of  $CO_2$  in the melt,  $fCO_2$  is fugacity in bar, and  $T$  temperature and  $R$  gas constant in SI units. The exponential function on the right hand side is known as the Poynting factor, which captures the influence of pressure and temperature on  $CO_2$  fugacity. The abundance of  $CO_2$  (ppmw) in melt is then

$$X_{CO_2} = 10^4 \left( \frac{4400 X_{CO_2}^m}{36.594 - 44 X_{CO_2}^m} \right). \quad (3)$$

This solubility law even compares favourably to experimental results at around 80 kbar ([Pan et al. 1991](#)), although such high pressures cannot be reached at the magma ocean surface of an Earth-sized terrestrial planet.

At water concentrations less than about 3 wt% there is a negligible influence of the presence of dissolved  $H_2O$  on  $CO_2$  solubility ([Dixon et al. 1995](#)). Above about 6 wt%, water can enhance the solubility of  $CO_2$  by around a factor of two ([Iacono-Marziano et al. 2012](#)), although  $CO_2$  remains comparatively insoluble compared to  $H_2O$ . In our model, the water concentration only increases beyond 3 wt% at the end of the magma ocean stage for the most oxidising condition and largest initial hydrogen budget: otherwise the water concentration is significantly less. Hence we ignore the minor influence of both carbon and hydrogen on each other's solubility.

### 2.2.3. Solubility of $H_2$ , $CO$ , and $CH_4$

We assume that the solubilities of  $H_2$ ,  $CO$ , and  $CH_4$  are negligible compared to  $H_2O$  and  $CO_2$ , respectively, and therefore set  $\alpha_{H_2} = \alpha_{CO} = \alpha_{CH_4} = 0$ . This is motivated by high pressure experiments that find the equilibrium constants for the dissolution of  $H_2$  gas in basaltic melts result in solubilities more than two orders of magnitude lower than that for  $H_2O$  (Li et al. 2015b; Hirschmann et al. 2012). Similarly, the mole fraction of reduced carbon dissolved in silicate melts is typically one to two orders of magnitude lower than for  $CO_2$  (Yoshioka et al. 2019).

Methane solubility was determined by Ardia et al. (2013) in Fe-free basaltic melts as a function of pressure between 0.7 and 3 GPa. The equilibrium constant of the reaction  $CH_4(l) = CH_4(g)$  results in an order of magnitude less dissolved C for a given  $fCH_4$  compared to an equivalent  $fCO_2$ . Because estimated  $CH_4$  contents are lower than several hundred ppm even at  $fCH_4$  of 1000 bar (Ardia et al. 2013) its solubility is neglected. It is noteworthy that solubility data for  $CH_4$  in silicate melts at low total pressures relevant to magma oceans ( $<0.7$  GPa) are lacking, preventing an accurate assessment of its solubility behaviour.

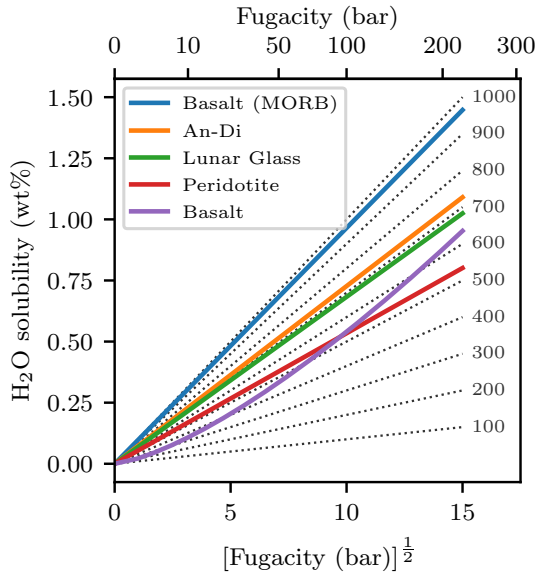
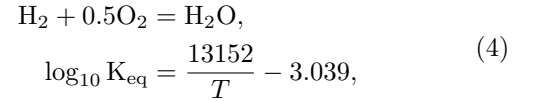


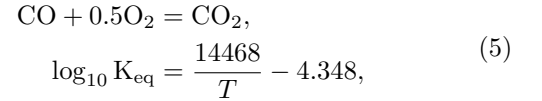
**Figure 1.** Experimentally-determined solubility data of  $H_2O$  for several melt compositions and temperatures, for fugacities from 0 to 200 bar (Table 1). Dotted lines denote  $\beta = 2.0$  and  $\alpha$  is reported at the end of the lines (Equation 1).

### 2.3. Redox reactions

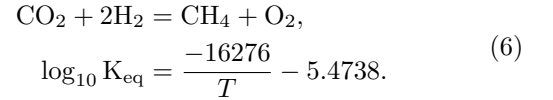
When at equilibrium, the magma ocean and atmosphere must be considered as a single thermodynamic unit. Accordingly, the  $fO_2$  defined by the magma ocean at its surface is equivalent to the oxygen partial pressure (or fugacity) in the atmosphere. Therefore, the fugacity ratio of gaseous redox couples ( $H_2/H_2O$  and  $CO/CO_2$ ), as well as  $CO_2$ - $H_2$ - $CH_4$ , satisfy chemical equilibrium at the  $T$  and  $fO_2$  imposed by the magma ocean at its surface. We consider three reactions, where all species exist in the gas phase albeit partially dissolved in the melt according to their respective solubilities (Sect. 2.2). For the hydrogen redox couple:



for the carbon redox couple:



and for  $CO_2$ - $H_2$ - $CH_4$ :



The equilibrium constants  $K_{eq}$  for the redox couples are determined from the Gibbs free energy of reaction using data from the JANAF database fit for temperatures between 1500 K and 3000 K (Chase 1998). The equilibrium constant for the  $CO_2$ - $H_2$ - $CH_4$  reaction is taken from the IVTANTHERMO database fit for temperatures between 300 K and 2000 K (Schaefer & Fegley 2017). The most abundant redox-sensitive element in the Earth's mantle is iron, so the amount of oxygen that is free to participate in reactions will be approximately regulated by Gibbs free energy changes along the iron-wüstite (IW) buffer during the magma ocean stage. Due to the presence of melt and the difficulty of determining the thermodynamic properties of a non-stoichiometric phase (wüstite), it is preferable to consider equilibrium of solid metallic Fe with liquid FeO (the IW buffer), where the Gibbs free energy of reaction constrains  $fO_2$  (O'Neill & Eggins 2002):

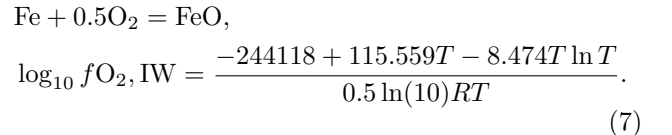


**Table 1.** H<sub>2</sub>O solubilities constrained by experimental studies

$\alpha^\ddagger$	$\beta$	Composition	Temp. (K)	Pres. (bar)	$f\text{O}_2$ ( $\Delta\text{IW}$ )	Reference
534	2.0	Peridotite	2173	1.013	-1.4 to +6.5	Sossi et al. (2021)
683	2.0	Lunar Glass	1623	1.013	-3.0 to +4.8	Newcombe et al. (2017)
727	2.0	Anorthite-Diopside	1623	1.013	-3.0 to +4.8	Newcombe et al. (2017)
965	2.0	Basalt (MORB)	1473	176 – 717	+3.9 to +13.2	Dixon et al. (1995)
1007	2.0	Basalt (MORB)	1473	503 – 2021	+3.5 and +7.9	Berndt et al. (2002)
215	1/0.7	Basalt	1373	1034 – 6067	unbuffered	Wilson & Head III (1981) <sup>†</sup>

NOTE—<sup>†</sup> Used in several modelling studies, e.g. Lebrun et al. (2013), Salvador et al. (2017), Nikolaou et al. (2019), and Bower et al. (2019). <sup>‡</sup>  $\alpha$  has units of ppmw/bar<sup>1/ $\beta$</sup>  and where relevant is determined by re-fits to existing data by constraining  $\beta = 2$  and no solubility at zero fugacity. We only consider experimental studies of basaltic or more mafic melts (i.e., Mg and Fe-rich) at relatively low  $f\text{H}_2\text{O}$  ( $\lesssim 2000$  bar).

It is convenient to define oxygen fugacity in log<sub>10</sub> units relative to the IW buffer ( $\Delta\text{IW}$ ):

$$\Delta\text{IW} = \log_{10} f\text{O}_2 - \log_{10} f\text{O}_{2,\text{IW}}. \quad (8)$$

In our nominal models we set  $\Delta\text{IW} = 0.5$  based on a recent determination of the inferred oxygen fugacity of Earth’s magma ocean at its surface using the Fe<sup>3+</sup>/Fe<sup>2+</sup> ratio from a global compilation of peridotites (Sossi et al. 2020). Hence by fixing  $f\text{O}_2$  relative to the IW buffer, H<sub>2</sub>O/H<sub>2</sub> (Equation 4) and CO<sub>2</sub>/CO (Equation 5) are constrained as a function of temperature, and by extension CH<sub>4</sub>/CO<sub>2</sub> (Equation 6). Therefore, while solubility controls the abundance of species in the atmosphere versus the interior, redox reactions dictate the relative abundance of oxidised to reduced species in the atmosphere. The thermodynamic coupling between the atmosphere and the interior is set by the surface temperature at the magma ocean–atmosphere interface. Appendices C.1 and C.3 describe how reactions are self-consistently incorporated into the time stepper that evolves the magma ocean–atmosphere system.

#### 2.4. Atmospheric escape

Atmospheric escape from terrestrial planets is challenging to parameterise given the complex interaction of thermal and non-thermal processes, as well as uncertainty regarding the history and details of the stellar environment and planetary magnetic field (e.g., Gronoff et al. 2020). In the context of this study, we concern ourselves with the impact of H<sub>2</sub> loss from the atmosphere on the evolution of the magma ocean–atmosphere system. We focus on hydrogen since it is the lightest atmospheric component and therefore the most prone to escape. Escape of H<sub>2</sub> may be buffered by outgassing from the interior resulting in efficient depletion of hydrogen from the magma ocean. We apply a model that obeys

an upper limit for H<sub>2</sub> loss based on the diffusion rate of H<sub>2</sub> through a hydrostatic carbon-dominated atmosphere (Zahnle et al. 2019). Below this limit, the escape flux follows the energy-limit which considers the stellar energy input necessary for a volatile to escape Earth’s gravitational field. Therefore, the H<sub>2</sub> escape flux is (Zahnle et al. 2019):

$$\phi_{\text{H}_2} \approx \frac{\gamma 10^{16} [\text{VMR}]_{\text{H}_2} S}{N_A \sqrt{1 + 0.006S^2}} \quad \text{moles m}^{-2} \text{ s}^{-1}, \quad (9)$$

where  $N_A$  is the Avogadro constant and  $[\text{VMR}]_{\text{H}_2}$  is the volume mixing ratio of H<sub>2</sub> which provides coupling between the evolving atmospheric speciation and H<sub>2</sub> escape. Here,  $\gamma$  is a scaling factor (unity by default) and  $S$  is the normalised solar irradiation according to Earth’s present-day value:

$$S(t) = F_{\text{xuv}}/F_{\text{xuv}\odot}, \quad (10)$$

where xuv combines the influence of X-rays, extreme ultraviolet, and far ultraviolet radiation. We adopt an upper estimate of  $S = 40$  at 4.0 Ga (Tu et al. 2015). For  $[\text{VMR}]_{\text{H}_2}$  of 30% and  $\gamma = 1$ , the H<sub>2</sub> mass loss rate is  $2.1 \times 10^5$  kg/s (Equation C12). Both the escape prefactor  $\gamma$  (constant for a given case) and  $[\text{VMR}]_{\text{H}_2}$  (time-dependent) scale the mass loss rate linearly.

## 3. RESULTS

### 3.1. Outgassing of hydrogen (one Earth ocean)

We first present magma ocean outgassing models (Case E1 and F1) where the total hydrogen (H) budget is equivalent to the mass of H in Earth’s present-day water ocean (hereinafter one ocean) (Figure 2). This budget is equivalent to a fully outgassed atmosphere of 270 bar for a single species atmosphere consisting of H<sub>2</sub>O. These

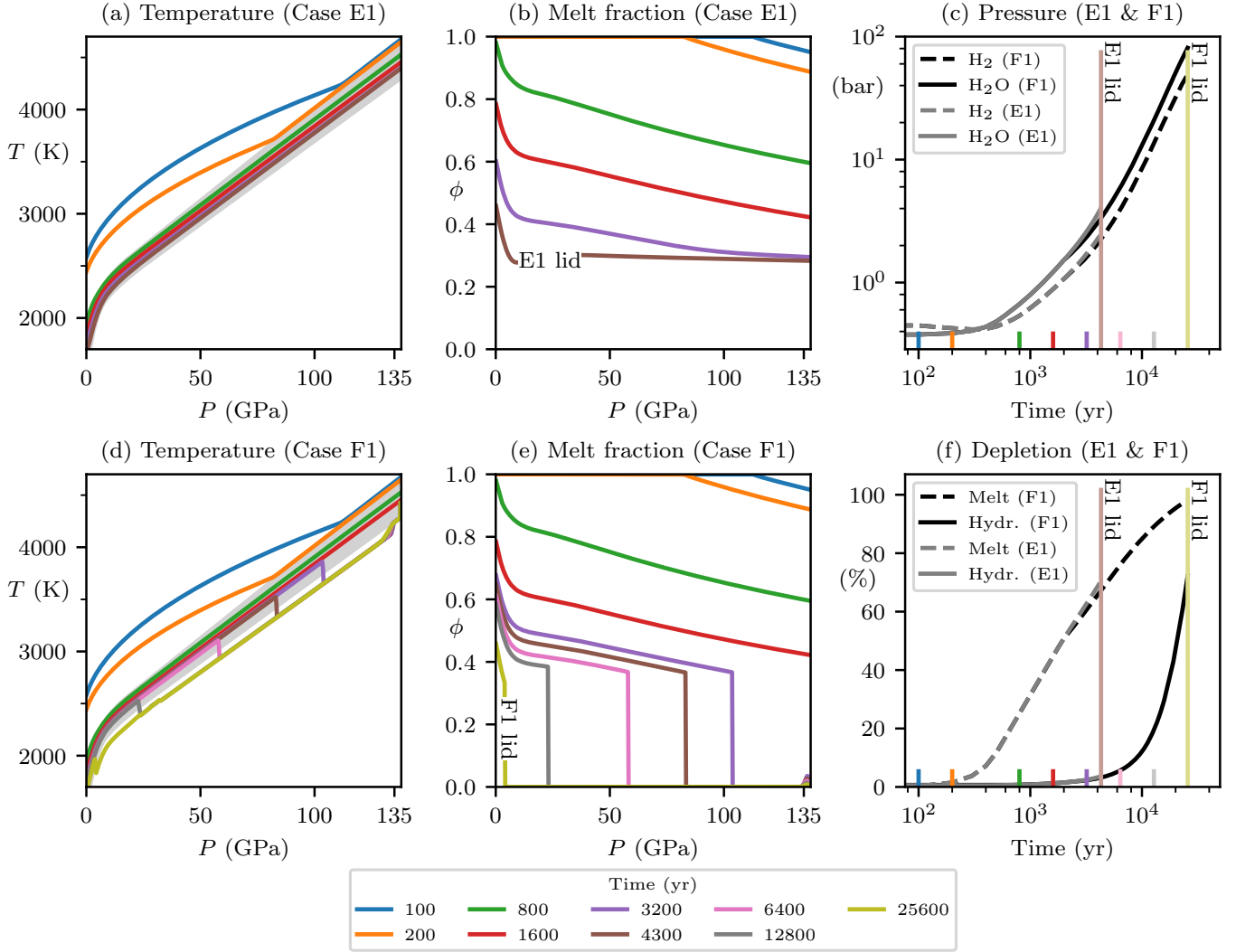


**Figure 2.** Coupled interior and atmosphere evolution during magma ocean outgassing at  $\Delta IW=0.5$  with a hydrogen budget of one Earth ocean (no carbon), where E1 shows equilibrium crystallisation and F1 shows fractional crystallisation. For E1 and F1: (a,d) Interior temperature with grey showing the mixed phase region where melt and solid coexist, (b,e) Interior melt fraction. (c) Atmospheric partial pressure of  $H_2$  and  $H_2O$  for E1 and F1, where the pressures of F1 (black lines) initially follow E1 (grey lines) before departing at late time. Colored vertical ticks and lines show times in (a,b,d,e) and labels show when a surface lid forms for E1 and F1. (f) Interior depletion of melt (‘Melt’) and hydrogen (‘Hydr.’) for E1 and F1.

models allow us to describe  $H_2$  and  $H_2O$  outgassing before subsequently introducing further complexity in the form of carbon species, redox variation, and atmospheric escape. The total budget of H is partitioned between a reduced ( $H_2$ ) and an oxidised ( $H_2O$ ) species according to the  $fO_2$  buffer set at  $\Delta IW=0.5$ , with an initial surface temperature of 2700 K. We recall that in our model  $H_2$  has zero solubility in the melt and so can only reside in the atmosphere. The only parameter difference between Case E1 (hereinafter E1) and Case F1 (hereinafter F1) is the crystal size, where  $a = 1$  mm for E1 and  $a = 5$  cm for F1. Both of these crystal sizes are reasonable for a crystallising magma ocean and demonstrate the end-member scenarios of equilibrium and fractional

crystallisation that arise depending on the efficiency of melt–solid separation which scales according to the crystal size squared (Appendix B).

Both E1 and F1 chart a similar thermal evolution when the melt fraction is high. Cooling proceeds quickly since most H remains in the magma ocean in the form of  $H_2O$ ; this keeps the atmospheric pressure low ( $< 1$  bar). The atmospheric composition (mole fraction of  $H_2$  compared to  $H_2O$ ) is determined by chemical equilibrium, where  $fO_2$  decreases with decreasing surface temperature (Equation 4) but parallels the IW buffer. Vigorous convection keeps crystals mostly in suspension assuming efficient reentrainment of crystals (Solomatov et al. 1993; Solomatov & Stevenson 1993a) and the interior is

approximately adiabatic. Due to the curvature of the melting curves and the two-phase adiabat, the deepest mantle has the lowest melt fraction and hence reaches the ‘rheological transition’ first. The rheological transition is defined by an abrupt increase in viscosity around 30–40% melt fraction, where the formation of an interconnected solid matrix begins to dictate the convective timescale. The ‘rheological front’ is the interface between melt-dominated dynamics above (lower pressure) and solid creep below (higher pressure), and moves upwards through the mantle as cooling proceeds. Hence convection in the deep mantle becomes sluggish akin to the present-day solid mantle, acting as a brake on deep mantle cooling (Andraut et al. 2016). Gravitational separation of melt and solid becomes a dominant driver of energy transport at the rheological transition (Abe 1993). Hence, the E1 and F1 models exhibit different interior and outgassing evolution because of the timescale of melt–solid separation (percolation) compared to net cooling rate.

E1 represents equilibrium crystallisation, where the timescale for melt–solid separation is longer than the timescale for the advancement of the rheological front (Tonks & Melosh 1990; Solomatov & Stevenson 1993b). The rheological front rapidly advances through the mantle causing the thermal profile to collapse on top of the rheological transition (Figure 2b). When it reaches the surface it initiates lid formation since convection has become so sluggish that heat transport by convection to the surface cannot prevent top-down cooling. Lid formation brings about the end of interior–atmosphere dissolution equilibrium (‘E1 lid’ at 4.3 kyr, Figure 2). At this time, the mantle is around 30% molten since it remains pinned at the rheological transition because it has not had time to undergo any significant differentiation through melt–solid separation prior to the formation of a surface lid. Therefore, the mantle contains sufficient melt to trap the majority of H as dissolved H<sub>2</sub>O beneath the surface lid (Figure 2f). Hence the subsequent interaction of these sequestered volatiles with the surface and atmosphere will be regulated by geological processes operating over long timescales (million to billion years), rather than by dissolution equilibrium with a comparatively short-lived magma ocean.

By contrast, for F1 the melt percolation velocity keeps pace with the upward velocity of the rheological front. This enables both the complete solidification of deep mantle layers below the rheological front by crystal settling, as well as stalling the upward progression of the rheological front. This occurs because efficient upward draining of melt keeps the upper regions molten at the expense of cooling and fully crystallising the lowermost

mantle (Figure 2e). Therefore, dissolution equilibrium with the atmosphere is maintained while crystals form and are displaced to depth. Hence F1 represents fractional crystallisation, where formed solids deep in the mantle can be considered chemically isolated from the molten reservoir above. Below the rheological transition, efficient melt–solid separation causes the thermal profile to abruptly drop to the solidus, where now subsolidus cooling is greatly restricted by the viscous transport timescale and partly by the core which buffers the cooling of the mantle (Figure 2d). This ultimately enables a substantial reduction of the melt reservoir (98% crystallised) at a surface temperature of 1650 K compared to E1 where the crystal fraction only reaches 70% (Figure 2f). Due to the high solubility of H<sub>2</sub>O in melt, for F1 the additional  $\approx 30\%$  crystallisation compared to E1 further depletes H from the interior by 65% before a surface lid forms. We note that fractional crystallisation could also occur for E1 after the surface lid has formed, but in this case the melt reservoir is separated from the atmosphere by a surface lid and therefore outgassing is not driven by dissolution equilibrium.

The atmospheric pressures of H<sub>2</sub>O and H<sub>2</sub> increase in unison during cooling (Figure 2c) because the relative abundance of these species is controlled by chemical equilibrium at  $\Delta IW=0.5$  (Equation 4). Since H<sub>2</sub>O is highly soluble in silicate liquid, early in the lifetime of the magma ocean (prior to 1 kyr while melt fractions are high) the atmospheric mass remains mostly constant and the partial pressures are controlled by the temperature-dependence of the  $fO_2$  buffer and equilibrium constant (Figure 2c, Equation 4). After 1 kyr, the extent to which H outgasses is proportional to the degree of crystallinity (i.e., continued cooling and crystallisation) according to the lever rule. Despite the mantle reaching 70% crystal fraction for E1 before a surface lid forms, the atmospheric pressures of H<sub>2</sub>O and H<sub>2</sub> only reach 4 bar and 2.4 bar, respectively (E1 lid, Figure 2c). For F1, the atmospheric pressures of H<sub>2</sub> and H<sub>2</sub>O (and hence their depletion in the magma ocean) track E1 until around 2 kyr (grey lines, Figure 2c,f). At this time, efficient melt–solid separation enables growth of a more substantial H<sub>2</sub>O (80 bar) and H<sub>2</sub> (50 bar) atmosphere prior to surface lid formation (‘F1 lid’, Figure 2c). It takes around 4.3 kyr and 26 kyr for a surface lid to form for E1 and F1, respectively, which compares favourably to a timescale of 10 kyr determined by a model with a more advanced treatment of radiative transfer (Lichtenberg et al. 2021). When a surface lid forms, the atmospheric pressure of E1 and F1 differs by more than an order of magnitude.

### 3.2. Outgassing of hydrogen (1–10 Earth oceans)

Planet formation models predict substantial delivery of water to the inner Solar System (Raymond & Izidoro 2017; Raymond et al. 2007), which can account for the 1–10 oceans of water currently stored in Earth (Lécuyer et al. 1998). Recent geochemical estimates propose around 2.5 oceans are currently stored in the mantle (Marty 2012; Hirschmann 2018). Therefore, we now present cases the same as E1 and F1 but with an initial H budget up to 10 Earth oceans. Since the main features of the coupled evolution of the interior–atmosphere are described for E1 and F1 (Section 3.1), only differences relative to these fiducial cases are now presented. Figure 3 reveals the interior depletion of H as a percentage of the H inventory, where the circles with a solid line and containing one are E1 (Figure 3a) and F1 (Figure 3b).

For both equilibrium and fractional crystallisation, as the H inventory is increased from 1 to 10 oceans the magma ocean lifetime increases by around two orders of magnitude, reaching a maximum duration slightly less than 1 Myr. This is because the optical depth of the atmosphere scales with pressure, and a larger inventory results in a larger outgassed atmosphere and hence a higher atmospheric pressure. Therefore, due to the thicker atmosphere, the magma ocean takes longer to cool before the rheological front reaches the surface and initiates lid formation. In addition, the interior depletion of H increases for larger total inventories as a direct consequence of power-law solubility where the exponent  $\beta = 2$ . This is because during cooling, the atmospheric reservoir of H grows with the water mole fraction to the second power (see Appendix C.6 for analysis). Hence for H outgassing, both the pressure of the atmosphere and relative depletion of the interior increases with the total inventory at a given melt fraction. For a volatile species that obeys a linear solubility relation ( $\beta = 1$ ), its relative depletion at a given melt fraction is independent of its total inventory (Appendix C.6). Water is expected to transition to such a linear solubility above around 10 ocean masses on the Earth due to the prevalence of dissolved  $\text{H}_2\text{O}$ .

For equilibrium crystallisation, lid formation occurs soon after 30% melt is reached (Figure 3a). For all equilibrium cases, melt–solid separation is slow compared to the cooling timescale so when a lid forms the melt fraction is only marginally reduced for cases with a long compared to a short cooling timescale. The magma ocean lifetimes for  $\Delta\text{IW} = 0.5$  cases (solid lines, Figure 3a) are comparable to cases that are fully oxidised where H can only exist as water (W cases, dashed lines, Figure 3a). This is because for all cases  $\text{H}_2\text{O}$  dominates the opacity of the atmosphere. However, H depletion

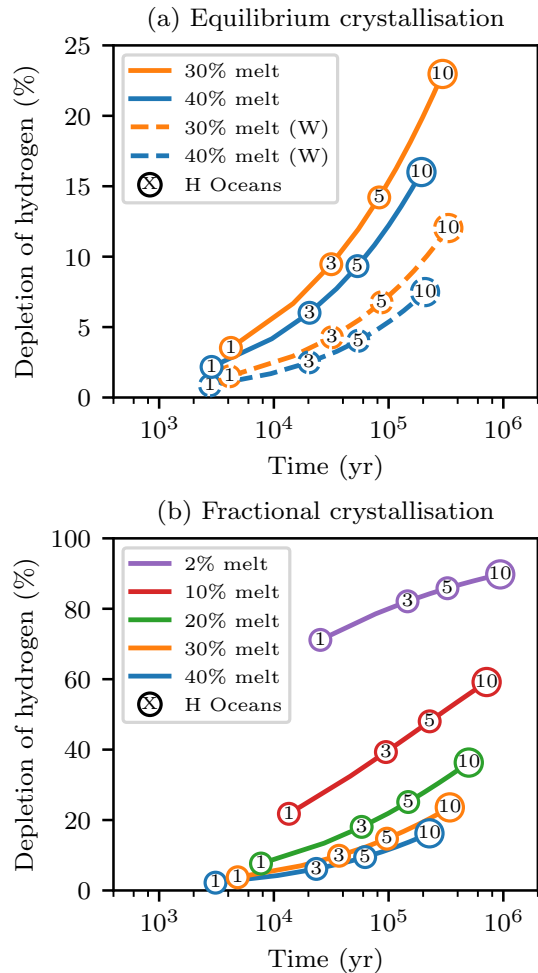


**Figure 3.** Depletion of hydrogen (H) from the interior during magma ocean outgassing at  $\Delta\text{IW}=0.5$  for H budgets from 1 to 10 Earth oceans: (a) Equilibrium crystallisation, and (b) Fractional crystallisation. Lines show constant melt fraction and circles show the H budget. Magma ocean stage ends at around 30% melt for equilibrium crystallisation and 2% melt for fractional crystallisation. Cases E1 and F1 (Figure 2) correspond to 1 H ocean for equilibrium and fractional crystallisation, respectively. Dashed lines in (a) with ‘W’ suffix denote models that only include H as  $\text{H}_2\text{O}$ , i.e. a completely oxidised mantle.

of the  $\Delta\text{IW}=0.5$  cases and the fully-oxidised (W) cases differ by up to about 11%. This is because at  $\Delta\text{IW}=0.5$ , outgassing of  $\text{H}_2\text{O}$  must be accompanied by commensurate growth of  $\text{H}_2$  in the atmosphere to maintain chemical equilibrium. Since the H budget is conserved, increasing  $\text{H}_2$  in the atmosphere necessitates a decrease in the  $\text{H}_2\text{O}$  reservoir dissolved in the magma ocean.

In short,  $\text{H}_2\text{O}$  solubility determines  $\text{H}_2\text{O}$  outgassing, but oxygen fugacity dictates the additional depletion of interior hydrogen to maintain equilibrium between  $\text{H}_2$  and  $\text{H}_2\text{O}$  in the atmosphere. For fractional crys-

tallisation, lid formation occurs when the melt fraction drops below around 2%. Regardless of total inventory, depletion must tend to 100% when the melt fraction reaches zero because we assume no volatiles are retained in solids. This explains the flattening of the depletion curve for 2% melt fraction compared to, for example, 10% melt fraction.

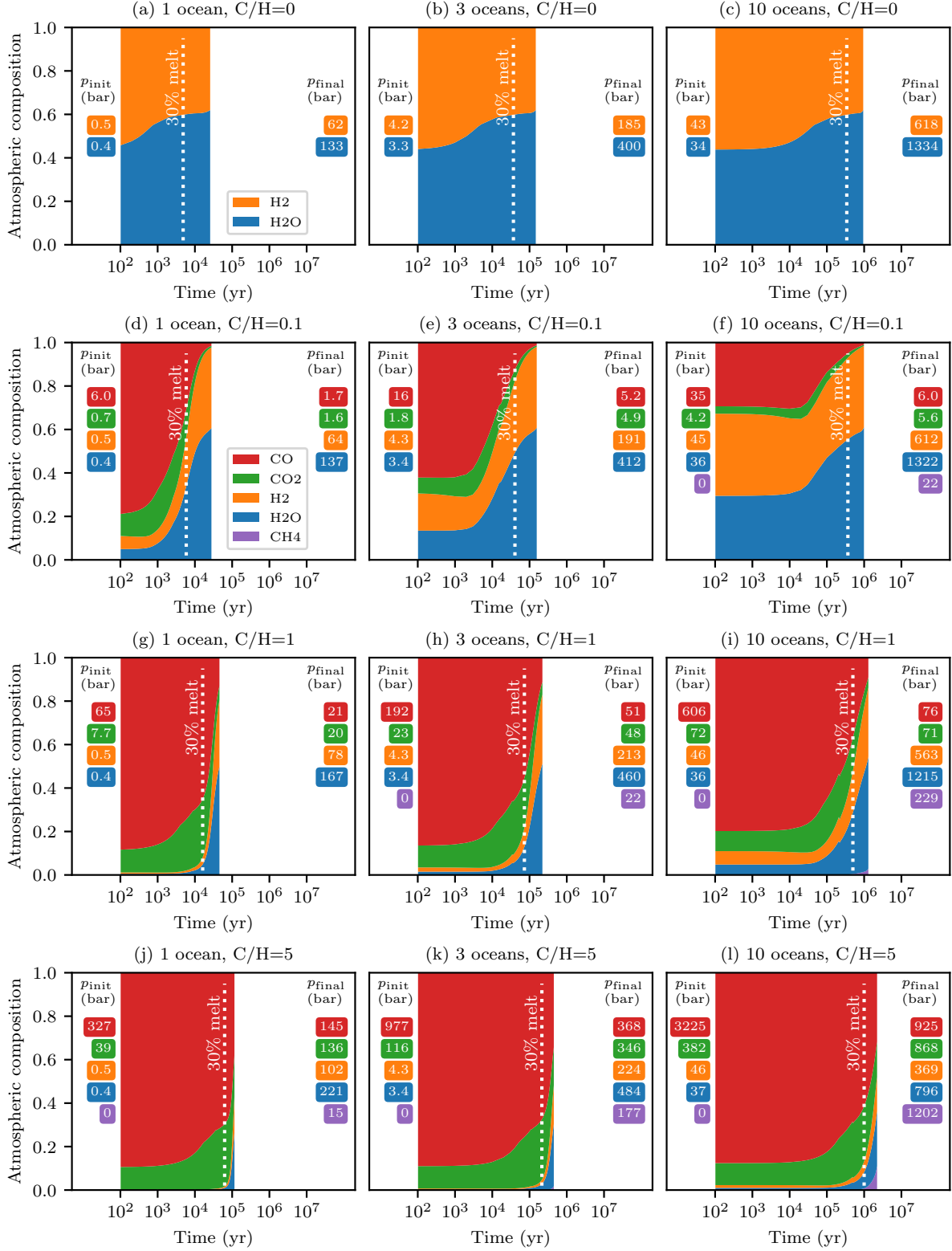
### 3.3. Outgassing of hydrogen and carbon

In contrast to the high solubility of water in silicate melt, carbon dioxide is relatively insoluble (e.g., Dixon et al. 1995). Hence, due to the high abundance of C in rocky planets, the presence of gaseous CO, CO<sub>2</sub>, and CH<sub>4</sub> may regulate the lifetime of a magma ocean and thereby the timescale over which H outgasses. Carbon also suppresses the outgassing of H through its influence on the mean molar mass of the atmosphere (Bower et al. 2019). Therefore, we now present fractional crystallisation cases that additionally include C species (CO<sub>2</sub>, CO, and CH<sub>4</sub>), with their relative abundances in the gas phase determined by redox reactions. The initial carbon to hydrogen ratio (C/H by weight) is varied from 0.1 to 5, which is a range compatible with C/H ratios in chondritic meteorites and in the bulk silicate Earth (1.1 and 1.4 by mass, respectively (Hirschmann 2016)).

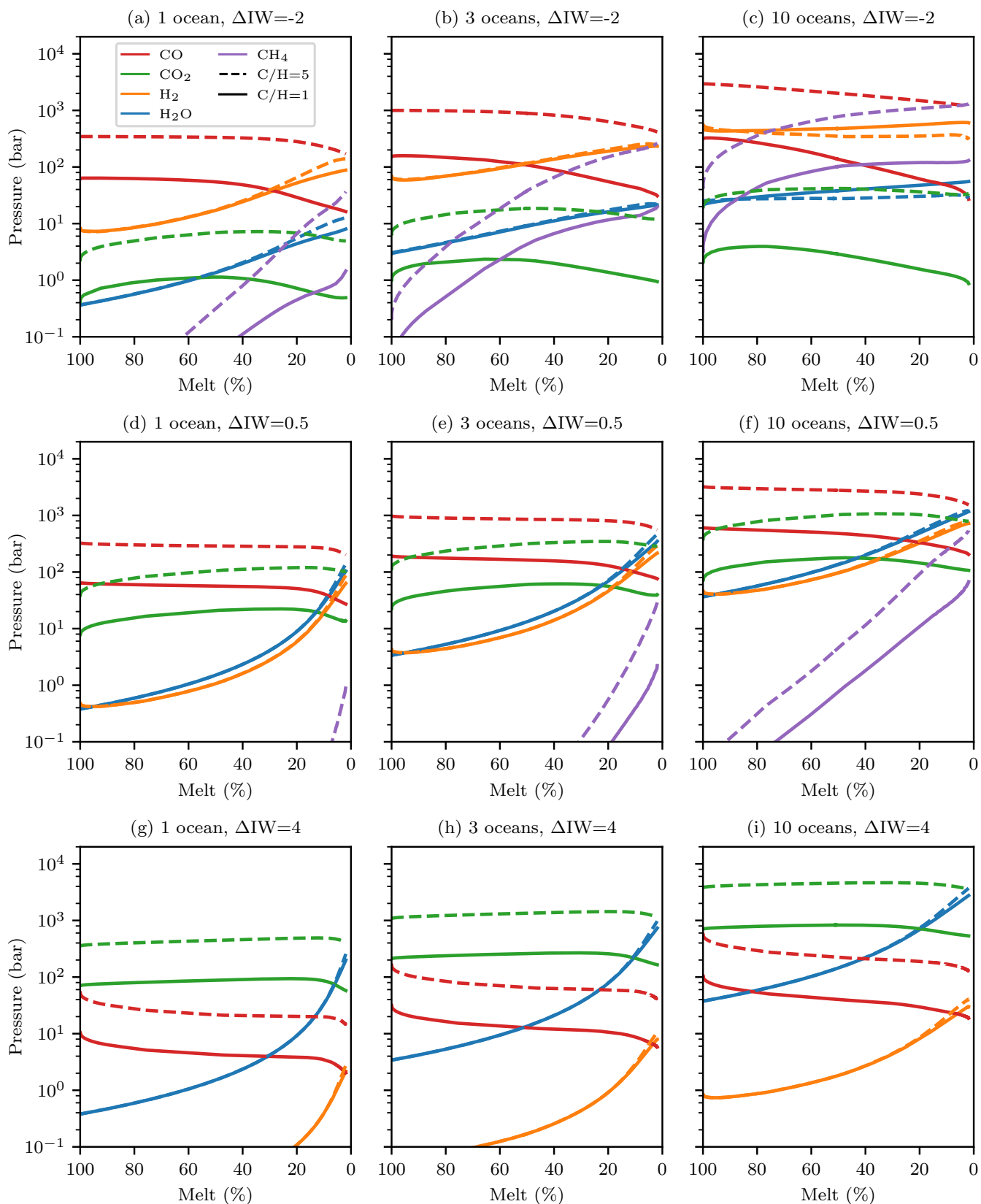
Figure 4 compares the influence of the C/H ratio on magma ocean outgassing for a H budget of 1, 3, and 10 oceans. Cases F1 (Figure 4a), F3 (Figure 4b), and F10 (Figure 4c) serve as carbon-free reference cases. We first focus attention on increasing C/H for a H budget of one ocean (left column, Figure 4). Even for an addition of only 10% C by weight (i.e., C/H=0.1), the atmosphere is dominated by C species (almost 90% volume mixing ratio) for a fully molten mantle. This is due to the low solubility of CO<sub>2</sub> compared to H<sub>2</sub>O, coupled with equilibrium chemistry that establishes the partial pressure of CO around a factor of seven greater than the partial pressure of CO<sub>2</sub>. During magma ocean cooling, the CO pressure in the atmosphere steadily decreases. This occurs due to the compounding effects of the equilibrium constant of Equation 5 that results in a decrease of  $f_{\text{CO}}/f_{\text{CO}_2}$  as the surface temperature decreases, and the continued outgassing of CO<sub>2</sub> as the melt fraction decreases. The latter also drives an initial increase in CO<sub>2</sub> pressure, although the CO<sub>2</sub> pressure decreases later once H begins to outgas in earnest. Hence even though the ever-decreasing melt fraction drives outgassing of both H and C throughout the magma ocean evolution, the partial pressure of volatile species can either mostly decrease (CO), mostly increase (H<sub>2</sub>, H<sub>2</sub>O), or increase then decrease (CO<sub>2</sub>) (Figure 5).

For a H budget of one ocean, the initial pressure of H<sub>2</sub> and H<sub>2</sub>O is 0.5 and 0.4 bar, respectively, regardless of C/H. However, at higher initial C/H ratios, the H species constitute a smaller fraction (volume mixing ratio) of the atmosphere due to the relative insolubility of C-bearing species compared to H<sub>2</sub>O. For C/H=5, hydrogen species constitute less than 1% of the atmosphere during the early evolution of the magma ocean (>30% melt). For this case, the mixing ratio of H species increases by a factor of 230 as the magma ocean cools from fully molten to fully solid (Figure 4j). In contrast, for C/H=0.1 the mixing ratio of H species only increases by a factor of about nine (Figure 4d). Even though the total inventory of H is fixed, the final outgassed pressures of H<sub>2</sub> and H<sub>2</sub>O depend on C/H, increasing from 62 bar and 133 bar (C/H=0) to 102 bar and 221 bar (C/H=5.0), respectively. White dotted lines in Figure 4 denote a melt fraction of 30%, which corresponds to when a surface lid forms for equilibrium crystallisation. Hence for equilibrium crystallisation, outgassed atmospheres are usually more dominated by C species versus H species. For C/H=0.1, the mixing ratio of H species increases by about a factor of two from 30% melt to 2% melt (Figure 4d). In contrast, for C/H=5, H species increase from about 1% to more than 50% over the same range of melt fraction (Figure 4j).

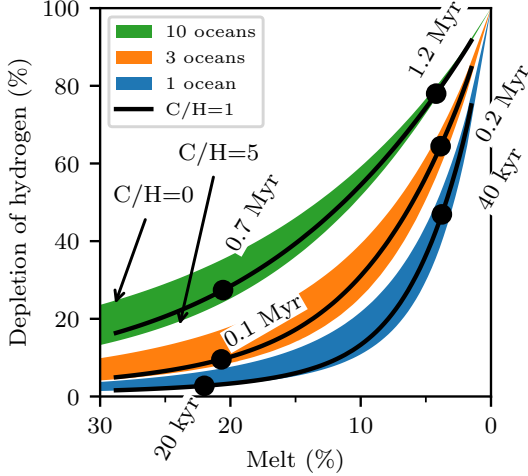
For an inventory of three oceans (middle column, Figure 4), a larger fraction of the atmosphere consists of H species during the evolution compared to an inventory of one ocean. This is a direct consequence of the power-law solubility of H<sub>2</sub>O and the higher amount of H (Appendix C.6). When no melt remains—as for the end of fractional crystallisation—the entire initial inventory of H and C sets the atmospheric composition where equilibrium chemistry continues to dictate the partitioning between reducing and oxidising species. Therefore, for fixed C/H at the end of fractional crystallisation, the volume mixing ratios are also set. If CH<sub>4</sub> is insignificant, the final partial pressures ( $p_{\text{final}}$ ) scale according to the initial inventory; for example, the final pressures for C/H=0.1 are a factor of three larger for a three ocean inventory compared to a one ocean inventory (compare  $p_{\text{final}}$  in Figure 4d,e). For large H inventories, the volume mixing ratio of H species changes less during outgassing because initially more H (compared to C) resides in the atmosphere due to the power-law solubility of H<sub>2</sub>O. The case with a three ocean budget and C/H=1 (Figure 4h, 5e) is similar to the bulk silicate Earth calculated in Sossi et al. (2020). At high temperatures, a CO-dominated atmosphere forms with ~200 bar C-bearing species and ~10 bar H-bearing species in which  $f_{\text{H}_2}$  and  $f_{\text{H}_2\text{O}}$  are subequal, while  $f_{\text{CO}} > f_{\text{CO}_2}$ .



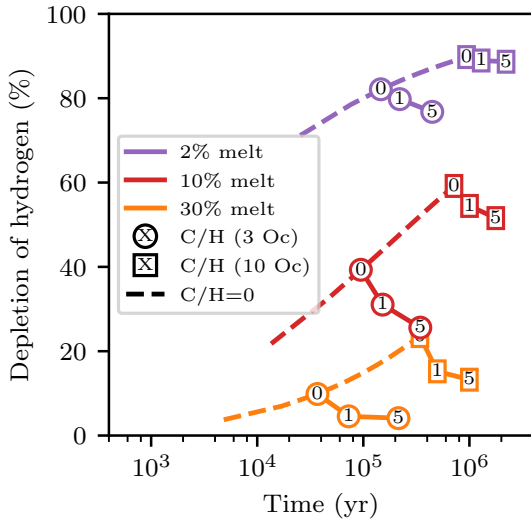
**Figure 4.** Atmospheric composition during magma ocean outgassing at  $\Delta IW=0.5$ . Columns from left to right show hydrogen (H) budgets of 1, 3, and 10 oceans, respectively. Rows from top to bottom show C/H by weight of zero, 0.1, 1, and 5. Magma ocean lifetime corresponds to the termination of the colored region (at  $\approx 2\%$  melt for fractional crystallisation, between  $10^4$  and  $10^7$  years). White dotted lines correspond to 30% melt, which indicates both the duration and atmospheric composition if instead the mantle underwent equilibrium crystallisation. Initial partial pressures of volatile species ( $p_{\text{init}}$ ) are for a completely molten magma ocean and  $T_{\text{surf}} = 2700$  K. Final partial pressures ( $p_{\text{final}}$ ) are for complete solidification and outgassing of all volatile species and  $T_{\text{surf}} = 1400$  K.



**Figure 5.** Atmospheric pressures during magma ocean outgassing for different C/H and  $f_{\text{O}_2}$ . Columns from left to right show hydrogen (H) budgets of 1, 3, and 10 oceans, respectively. Rows from top to bottom show  $f_{\text{O}_2}$  of  $\Delta\text{IW}=-2$ ,  $\Delta\text{IW}=0.5$ , and  $\Delta\text{IW}=4$ . Colors denote volatiles (red: CO, green:  $\text{CO}_2$ , orange:  $\text{H}_2$ , blue:  $\text{H}_2\text{O}$ , purple:  $\text{CH}_4$ ), where solid lines show C/H=1 and dashed lines show C/H=5.



**Figure 6.** Depletion of hydrogen (H) vs. melt fraction at  $\Delta IW=0.5$  for H budgets of 1, 3, and 10 oceans and different C/H by weight. For each shaded region, the upper bound is C/H=0, lower bound is C/H=5, and black line is C/H=1. Symbols indicate times of C/H=1 cases near 20% melt and 5% melt.



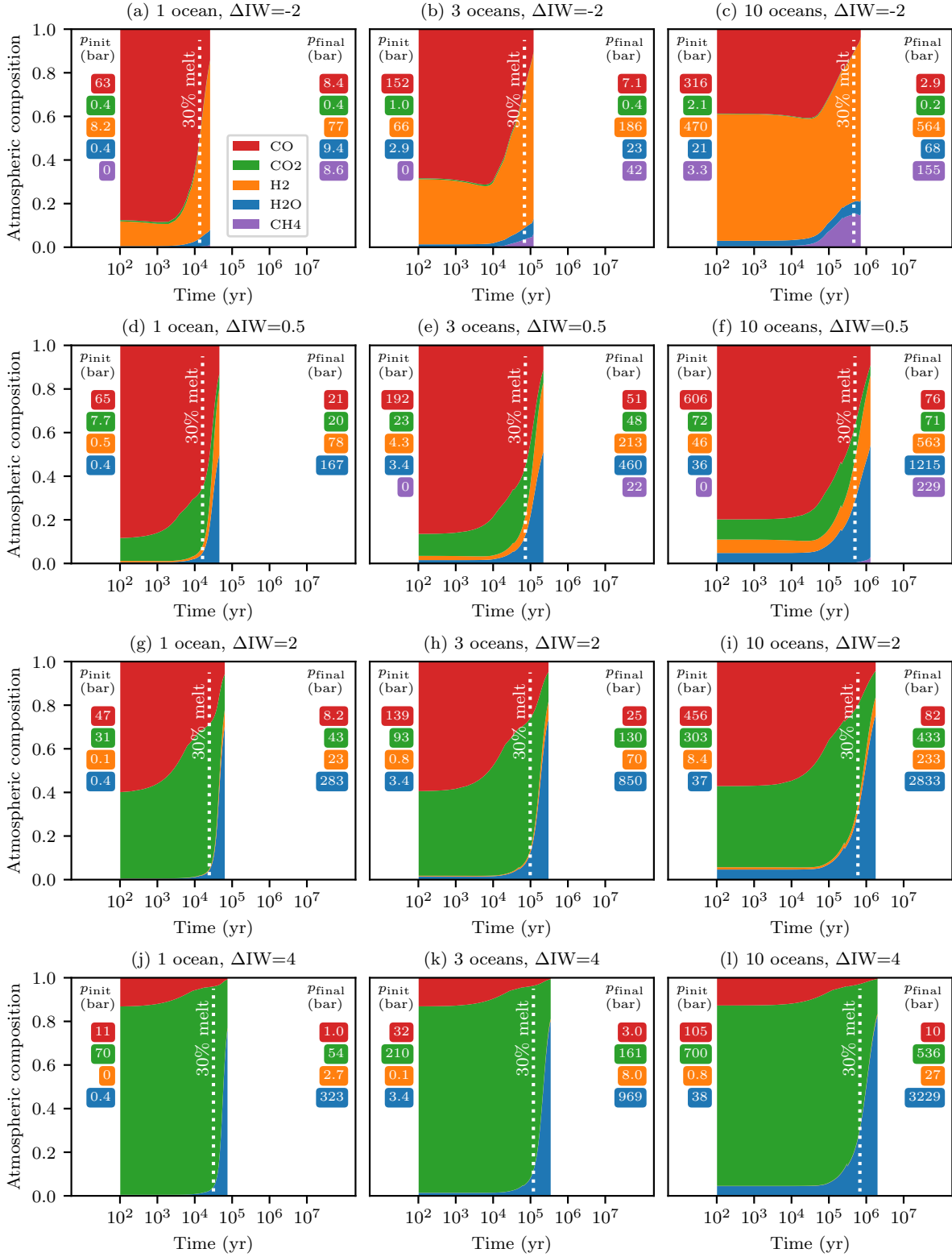
**Figure 7.** Depletion of hydrogen (H) vs. time at  $\Delta IW=0.5$  for different C/H, where colored lines show constant melt fraction. Dashed lines show C/H=0 for H budgets from 1 to 10 Earth oceans; these are the solid lines in Figure 3b. Departing from the dashed lines, circles show 3 oceans and C/H=X, where X is zero, 1, or 5. Similarly, rectangles show 10 oceans and C/H=X, where X is zero, 1, or 5.

Figure 6 summarises the interior depletion of H for 1–10 oceans and C/H by weight varying from zero to five. To first order, depletion at a given melt fraction is dictated by the total inventory of H due to the power-law solubility of  $H_2O$ . For 10% melt, this gives rise to around a 40% increase in depletion as the H inventory increases

from 1 to 10 oceans. A secondary influence on depletion is C/H, where higher C/H suppresses the outgassing and hence depletion of H. This effect is not connected to the solubility of  $H_2O$ , but rather is due to the dominant presence of C species in the atmosphere that increases the mean molar mass of the atmosphere relative to H species (Appendix C.1). Figure 7 reveals the influence of C/H on the depletion during magma ocean outgassing and can be compared with Figure 3. For a fixed H inventory, increasing C/H prolongs the time taken to reach a given melt fraction since the optical depth of the atmosphere increases. Increasing C/H increases the volume mixing ratio of C species in the atmosphere, and this alone would actually decrease the opacity of the atmosphere since CO has the lowest opacity of all the considered volatiles (Appendix A). However, increasing C/H also increases the total surface pressure substantially because  $CO_2$  is relatively insoluble compared to  $H_2O$ . Hence the optical depth increases in response to the larger surface pressure and this increase predominates over the change in speciation; the net outcome is prolonged cooling for larger C/H. Figure 7 further demonstrates the trend of Figure 6, in which increasing C/H suppresses the outgassing and hence interior depletion of H at a given melt fraction.

### 3.4. Oxygen fugacity

Iron core formation established the deep Earth’s redox state at  $\Delta IW=-2$  whereas the present-day upper mantle redox is  $\Delta IW=4$ . This indicates that mantle redox can vary with both time (e.g., Scaillet & Gaillard 2011) and pressure (Armstrong et al. 2019), potentially giving rise to atmospheres that are more reduced or oxidised than our nominal cases at  $\Delta IW=0.5$  (e.g., Hirschmann 2012). Hence we supplement our calculations at  $\Delta IW=0.5$  by additionally considering outgassing scenarios at  $\Delta IW=-2$ ,  $\Delta IW=2$ , and  $\Delta IW=4$ . Figure 8 summarises the results for C/H=1 and detailed figures for all C/H cases at each  $fO_2$  are presented in Appendix D. Increasing the oxygen fugacity from  $\Delta IW=0.5$  to  $\Delta IW=4$  progressively increases the ratio of oxidised to reduced species in the atmosphere at a given temperature. Since oxidised species of C and H have a higher molar mass than their reduced counterparts, this also increases the mean molar mass of the atmosphere which influences partial pressures through mass balance (e.g., Equation C9). Cooling times are generally extended for oxidised versus reduced atmospheres, due to the higher surface pressure and the intrinsic higher opacity of oxidised species (Appendix A). However, for  $\Delta IW=-2$  and C/H=5, production of  $CH_4$



**Figure 8.** Atmospheric composition during magma ocean outgassing for  $C/H=1$  and different  $fO_2$ . Columns from left to right show hydrogen (H) budgets of 1, 3, and 10 oceans, respectively. Rows from top to bottom show  $fO_2$  of  $\Delta IW = -2$ ,  $\Delta IW = 0.5$ ,  $\Delta IW = 2$ , and  $\Delta IW = 4$ . Magma ocean lifetime corresponds to the termination of the colored region (at  $\approx 2\%$  melt for fractional crystallisation, between  $10^4$  and  $10^7$  years). White dotted lines correspond to 30% melt, which indicates both the duration and atmospheric composition if instead the mantle underwent equilibrium crystallisation. Initial volatile partial pressures ( $p_{init}$ ) are for a completely molten magma ocean and  $T_{surf} = 2700$  K. Final partial pressures ( $p_{final}$ ) are for complete solidification and outgassing of all volatiles and  $T_{surf} = 1400$  K.

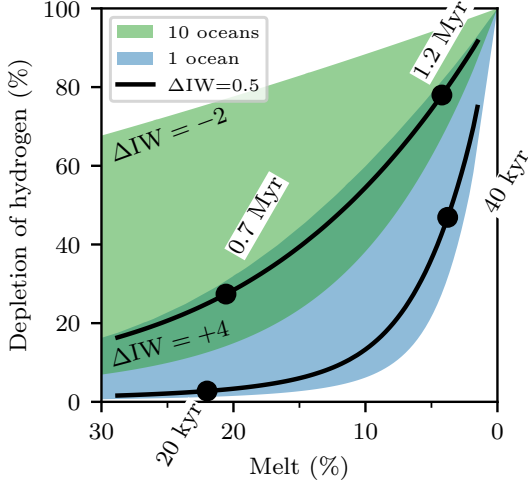


**Figure 9.** Depletion of hydrogen (H) vs. melt fraction for H budgets of 1 and 10 oceans and different  $fO_2$ . For each shaded region, the upper bound is  $\Delta IW = -2$ , lower bound is  $\Delta IW = 4$ , and black line (same as Figure 6) is  $\Delta IW = 0.5$ . Symbols indicate times of  $\Delta IW = 0.5$  cases near 20% and 5% melt.

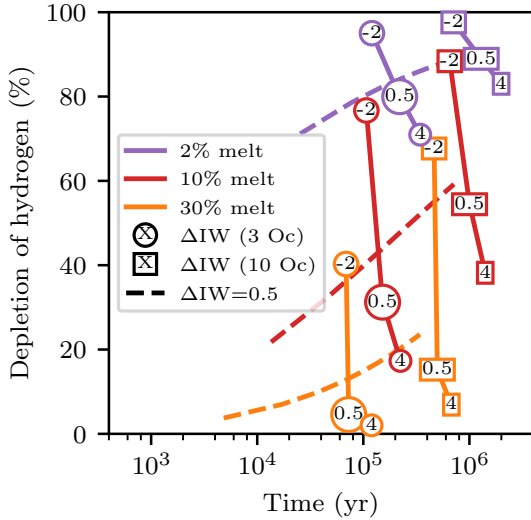


**Figure 10.** Depletion of hydrogen (H) vs. time for different  $fO_2$ , where colored lines show constant melt fraction. Dashed lines show  $\Delta IW = 0.5$  and  $C/H = 0$  for H budgets from 1 to 10 Earth oceans; these are the solid lines in Figure 3b. Departing from the dashed lines, circles show 3 oceans and  $C/H = 1$  for  $\Delta IW = X$ , where  $X$  is  $-2$ ,  $0.5$ , or  $4$ . Similarly, rectangles show 10 oceans and  $C/H = 1$  for  $\Delta IW = X$ , where  $X$  is  $-2$ ,  $0.5$ , or  $4$ .

increases the cooling time to be comparable to an oxidised atmosphere dominated by  $CO_2$  and  $H_2O$ .

Oxidised interiors mitigate the interior depletion of H relative to reducing conditions (e.g., compare  $\Delta IW = -2$  and  $\Delta IW = 4$  in Figure 9 and 10). At 30% melt, H deple-

tion is around a factor of ten larger for  $\Delta IW = -2$  compared to  $\Delta IW = 4$ . At 2% melt, H depletion at  $\Delta IW = -2$  is approximately 20% larger than  $\Delta IW = 4$ ; we recall that depletion for all cases must reach 100% when no melt remains. Depletion of H is largest for  $\Delta IW = -2$  because it exists mainly as the less soluble  $H_2$  and  $CH_4$  in the gas, so only a small quantity of H is dissolved in the melt reservoir as  $H_2O$ . Whereas increasing  $C/H$  mitigates H depletion and extends cooling times, decreasing  $fO_2$  greatly enhances H depletion (i.e., outgassing) and generally reduces cooling times. For  $C/H = 1$ , early atmospheres are almost always dominated by carbon species, either as  $CO$  (reduced cases) or  $CO_2$  (oxidised cases). For 10 H oceans and  $\Delta IW = -2$  the early atmosphere is instead dominated by  $H_2$ . Even for the most oxidised scenario when  $\Delta IW = 4$ ,  $H_2O$  is never the dominant species in the atmosphere until the melt fraction drops below about 20% or even less. Hence magma oceans that undergo fractional crystallisation are more likely to produce oxidised and  $H_2O$ -rich atmospheres versus equilibrium crystallisation which produces reduced and often  $CO$ -rich atmospheres.

### 3.5. Atmospheric escape of H during outgassing

During the magma ocean stage, escape of  $H_2$ —the lightest atmospheric component—could impact the reservoir evolution of volatiles, so we explore this possibility in Figure 11. The reference case has  $C/H = 0.1$ , 3 H oceans and unity escape prefactor ( $\gamma = 1$ , Equation 9). However, an equivalent case with no escape is visually indistinguishable from  $\gamma = 1$ . This immediately demonstrates that  $H_2$  escape due to irradiation of a carbon–hydrogen atmosphere does not appreciably alter the volatile reservoirs during the magma ocean stage for an Earth-sized body at 1 AU, largely because of the magma ocean’s short lifetime ( $\sim 10^5$  yr). Even for a larger H budget of 10 oceans where cooling is relatively prolonged,  $\gamma \lesssim 100$  has no appreciable impact on the evolution of the volatile reservoirs. Therefore, we show a case in which escape is increased by setting  $\gamma = 1000$  (‘large escape’) to investigate an extreme end-member escape scenario, which may arise for example due to tidal effects. For comparison,  $\gamma = 1000$  gives a mass loss rate around  $2.1 \times 10^8$  kg/s, which is within the range of rates determined for volatile stripping of the proto-Moon by the Earth (Charnoz et al. 2021) or for a Mars-sized body near 1 AU undergoing EUV-driven thermal escape (Benedikt et al. 2020). For large escape the inventory of hydrogen decreases by almost 50% over the lifetime of the magma ocean of around  $10^5$  years. By comparison, the magma ocean lifetime for an equivalent case without escape is around  $1.5 \times 10^5$  years.

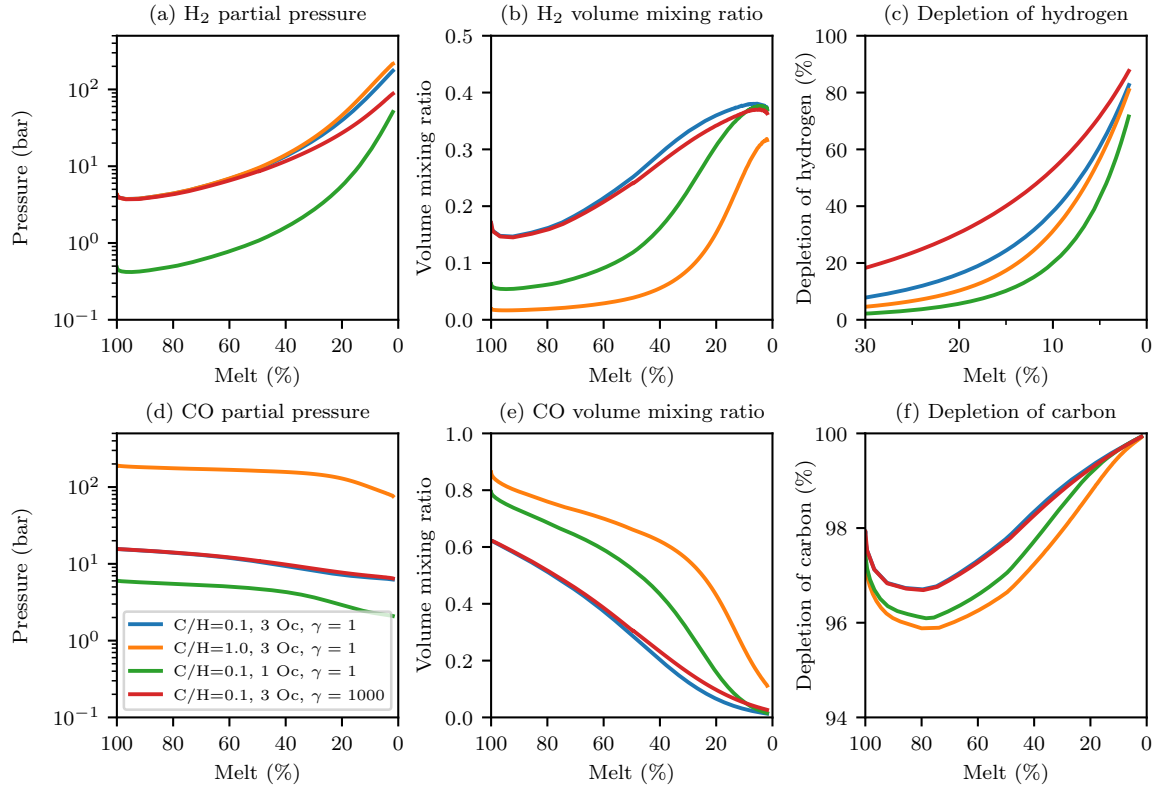


**Figure 11.** Comparison of atmospheric composition and interior depletion at  $\Delta IW=0.5$  for (1)  $C/H=0.1$ , 3 H oceans,  $\gamma = 1$  (2)  $C/H=1.0$ , 3 H oceans,  $\gamma = 1$  (3)  $C/H=0.1$ , 1 H ocean,  $\gamma = 1$  and (4) ‘Large escape’ with  $C/H=0.1$ , 3 H oceans, and an escape prefactor  $\gamma = 1000$  (Equation 9). (a,b)  $H_2$  partial pressure and volume mixing ratio, (d,e) CO partial pressure and volume mixing ratio, (c,f) Interior depletion of H and C, respectively.

Early on (equivalently times at which melt  $>40\%$ ), the  $H_2$  partial pressure of all cases with 3 H oceans follows a comparable trajectory. At later times (equivalently  $<40\%$  melt), the cases with 3 oceans and  $\gamma = 1$  continue to track a similar trend, although the final  $H_2$  partial pressure depends on the initial  $C/H$  (e.g., Figure 4e,h). For high escape rate, however, the growth of  $H_2$  in the atmosphere is mitigated by escape such that the  $H_2$  partial pressure is reduced compared to the cases with an unchanging H inventory of 3 oceans. Nevertheless, equilibrium chemistry continues to dictate  $f_{H_2}/f_{H_2O}$  so only the magnitude of the partial pressures of H species are modulated by escape. The buffering of the atmosphere by the magma ocean presupposes that the loss of  $H_2$  is not sufficient to influence the redox state of the magma ocean itself. In practice, the preferential loss of  $H_2$  promotes oxidation of the residual mantle (e.g., Olson & Sharp 2019). The precise amount depends on the abundance of H, but the net effect is to self-arrest loss of H as  $H_2$ . This is because as escape proceeds, necessarily more  $H_2$  is converted to  $H_2O$ , given that O-bearing species are heavier and thus escape less readily than  $H_2$ . Since for large escape almost 50% of the initial 3 ocean inventory is lost,  $f_{H_2}$  is steered towards the final pres-

sure (at 0% melt) of the one ocean case, which has the same  $C/H=0.1$ . For fixed  $C/H=0.1$ , the volume mixing ratio of  $H_2$  is the same at 0% melt regardless of the final H inventory. However, for large escape, H is lost relative to C, and hence the  $H_2$  volume mixing ratio at the end of the magma ocean stage is slightly reduced compared to cases with unchanging  $C/H=0.1$ .

Atmospheric escape modulates two controls on outgassing during magma ocean cooling that we have previously investigated: (1) escape decreases the inventory of H and hence modulates the partitioning of H between the interior and atmosphere when melt is present according to the power-law solubility of  $H_2O$ , and (2) escape increases  $C/H$ , resulting in a final atmosphere richer in C compared to H. For example, the loss of  $H_2$  for large escape increases the volume mixing ratio of CO at later time compared to  $C/H=0.1$ . This abides by our previous models that show a larger contribution of carbon species to the atmosphere for a larger  $C/H$ . For large escape,  $C/H$  by weight increases from 0.1 initially to 0.2 at the end of the magma ocean stage. For minimal escape, both decreasing the H inventory and/or increasing  $C/H$  suppresses the interior depletion of H at a given melt fraction, relative to the total inventory (Figure 6).

However, for large escape, the depletion of H is enhanced relative to other cases (Figure 11). This demonstrates that the direct loss of H due to escape is a stronger control on its depletion in the magma ocean than the secondary effects on its solubility (through H inventory) and the suppression of H outgassing due to a heavier, carbon-rich atmosphere. In short, H<sub>2</sub> escape driven by irradiation given best estimates for the XUV flux of the young Sun has an insignificant impact on volatile reservoir evolution of an Earth-sized body at 1 AU during the magma ocean stage. However, more extreme escape scenarios can reduce the partial pressure of H species in the atmosphere and drive faster depletion of the interior H reservoir.

## 4. DISCUSSION

### 4.1. Atmospheric composition and evolution

For a redox state inferred for the early Earth, the earliest outgassed atmospheres of terrestrial planets are dominantly CO-rich by volume mixing ratio when the mantle is mostly molten (Figure 12). This is borne out of the equilibrium chemistry of CO–CO<sub>2</sub> and the low solubility of C species compared to H species. With C present, H species can in principle constitute more than 50% of the atmosphere if the H budget is greater than about 6 Earth oceans due to the power-law solubility of H<sub>2</sub>O. However, this is only possible if C/H by weight is low—around an order of magnitude less than for the bulk silicate Earth. As C/H increases to unity (Earth-like) and beyond, the atmosphere is CO-rich regardless of the H budget. Hence only for  $C/H \lesssim 0.1$  is a H-rich atmosphere dominant during the early cooling phase when most of the mantle is molten. Throughout the magma ocean stage, H<sub>2</sub> and H<sub>2</sub>O have roughly constant mixing ratios owing to the weak temperature dependence of the equilibrium constant (Equation 4), while  $f_{H_2}/f_{H_2O}$  is approximately unity at  $\Delta IW=0.5$  at magmatic temperatures.

For  $C/H \gtrsim 1$ , H species can only begin outgassing in earnest once the melt fraction drops below about 30%, regardless of the redox state. However, this is contingent on the surface remaining molten to ensure equilibrium between the interior and atmosphere; this is less likely if the magma ocean undergoes equilibrium crystallisation where crystals and melt freeze together and a surface lid forms quickly. In comparison, fractional crystallisation—driven by melt–solid separation—can more likely maintain a molten surface while the deeper mantle crystallises and exsolves volatiles. Hence, the transition from a C-rich to H-rich atmosphere depends on the style of crystallisation, and crucially the behaviour of the mantle as it transitions from mostly

molten to mostly solid. A large steam-dominated atmosphere can only form for a relatively oxidised mantle towards the end of mantle crystallisation, although it may persist for a longer duration than the early carbon-rich atmosphere in the absence of an efficient loss mechanism. An atmosphere that contains initially more H species by volume mixing ratio ( $C/H \lesssim 0.1$  and particularly for H inventories  $> 6$  oceans) undergoes less modification during outgassing to reach its final volatile mixing ratios when the mantle has fully crystallised.

### 4.2. Hydrogen retention

In order for otherwise highly soluble volatiles, such as H<sub>2</sub>O, to exist in the atmosphere, the magma ocean must have crystallised beyond 30% melt fraction, before a surface lid could form and persist at the surface. Otherwise, thermodynamic communication between the interior and atmosphere is broken and dissolved volatiles remain trapped in the mantle. Outgassing of dissolved volatiles requires that significant solidification occurs through melt percolation and solid compaction before the rheological front reaches the surface (fractional crystallisation). At a given melt fraction, we find that a larger fraction of H can be retained for smaller total inventories of H, larger C/H by weight, and more oxidised interiors. Although C does not influence H solubility directly, it impacts H retention since it suppresses H outgassing through its influence on the mean molar mass of the atmosphere.

Equilibrium crystallisation results in a substantial reservoir of melt and hence volatiles trapped in the interior when the surface forms a lid. This later possibility has received less attention in the context of volatile evolution during the magma ocean stage, but provides a mechanism to safely harbour a significant quantity of volatiles in the mantle to protect against loss from atmospheric escape and impacts. Hence the high solubility of H<sub>2</sub>O in silicate melt may be a crucial property of this life-supporting molecule that enables it to survive during the violent early years of a terrestrial planet’s life.

Volatile retention would be further enhanced if a melt–crystal density crossover enabled the formation of a voluminous basal magma ocean (Labrosse et al. 2007; Caracas et al. 2019) or if melt is captured as the rheological front advances through the mantle (Hier-Majumder & Hirschmann 2017). Trapped melt, and hence soluble volatiles, could then be sequestered in the deep mantle by Rayleigh-Taylor instability (Maurice et al. 2017; Miyazaki & Korenaga 2021). These factors further conspire against the wholesale degassing of soluble volatiles, namely water, during the magma ocean stage. Moreover, we assume no solubility of H in crystallising

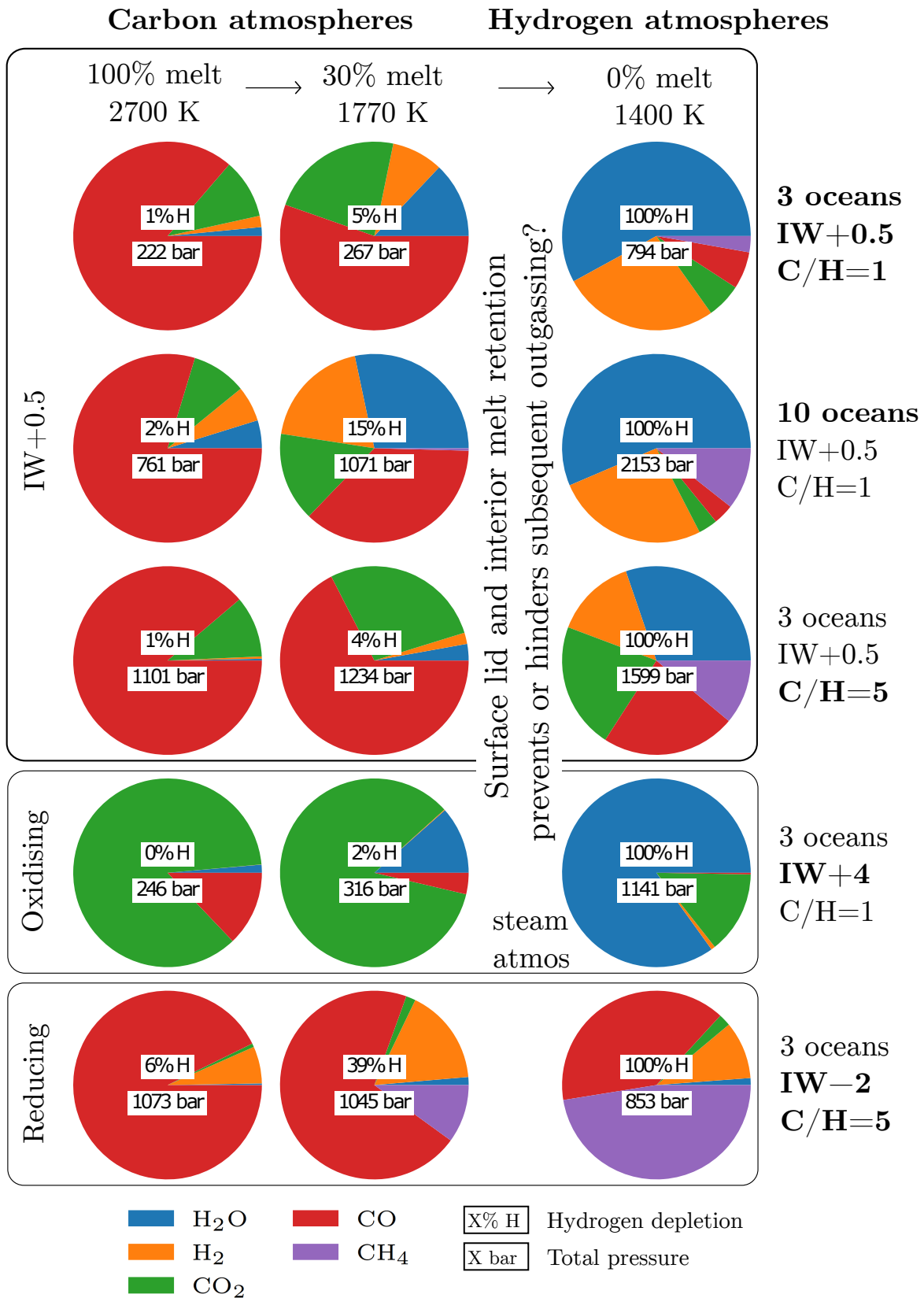


**Figure 12.** Summary of atmospheric composition and hydrogen depletion of the interior during magma ocean cooling at 100%, 30%, and 0% melt, where the surface temperature is given below the melt fraction. Transition from carbon-dominated to hydrogen-dominated atmospheres depends on surface lid formation and the style of magma ocean crystallisation, which may prevent or hinder interior outgassing below 30% melt fraction.

minerals, whereas experimental data indicate significant quantities of water may be stored in ringwoodite (Fei & Katsura 2020). Hence a large trapped reservoir of H<sub>2</sub>O in the interior may interact with the surface environment and atmosphere over geological timescales (million to billion years) following surface lid formation. The detailed chemical and physical processes governing the formation and sustenance of a surface lid require further investigation; for example, external influences such as projectile bombardment could stifle lid formation (e.g., Perera et al. 2018).

For an Earth-like planet orbiting a Sun-like star at 1 AU during its magma ocean stage, we find that atmospheric escape of H<sub>2</sub> due to irradiation (energy and diffusion limited) does not significantly impact the evolution of volatile reservoirs, in agreement with Hamano et al. (2013); Katyal et al. (2020). This is because escape rates are sufficiently low and the magma ocean duration sufficiently short (at most a few million years). In future work, a feedback to probe is that loss of H<sub>2</sub> increases  $f\text{O}_2$  slightly, causing more H<sub>2</sub> to convert to H<sub>2</sub>O and thereby partly self-arresting the loss process. Furthermore, we have not considered photodissociation of H<sub>2</sub>O, but this could interplay with the included geochemical reactions that depend on mantle redox.

#### 4.3. Crystallisation style

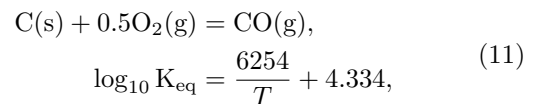
Based on energetic considerations of convection versus gravitational settling, Solomatov & Stevenson (1993a) propose a critical crystal size of 1 cm above which fractional crystallisation is inevitable. Furthermore, they show that the critical crystal size is weakly dependent on crystal fraction and therefore depth. Hence their results are compatible with our fractional crystallisation models with a constant crystal size of 5 cm. In detail, gravitational settling in our models becomes dominant at the rheological transition due to the substantial decrease of turbulence that enabled crystals to remain mostly in suspension. It is reasonable to assume that crystals are suspended at high melt fraction (Tonks & Melosh 1990), although they could begin to settle and thereby initiate fractional crystallisation before the rheological transition is obtained (Patočka et al. 2020), assuming inefficient re-entrainment (Solomatov et al. 1993) or a high planetary rotation rate (Maas & Hansen 2019). Settling also depends on mineral buoyancy, and if the minerals float rather than sink, this could hinder interior–atmosphere communication. For example, preferential partitioning of Fe into melt during crystallisation continuously changes the level of neutral buoyancy between crystals and melt (Caracas et al. 2019). In contrast to fractional crystallisation, equilibrium crystallisation

prevents differentiation of the mantle and occurs for a smaller crystal size of 1 mm (Solomatov & Stevenson 1993b).

Most previous dynamic models of magma ocean cooling do not consider melt–solid separation (Lebrun et al. 2013; Hamano et al. 2013; Schaefer et al. 2016; Nikolaou et al. 2019); rather, the interior is assumed to always be adiabatic. Yet some of these previous models report agreement with the solidification timescale derived from geochemical models that explicitly consider fractional crystallisation. The previous models implicitly assume that although the deep mantle reaches the rheological transition first, it continues cooling as efficiently by convection as the uppermost mantle; this allows the melt fraction to continue decreasing at a similar rate. However, this is unlikely given the rheological behaviour of a melt–solid aggregate (e.g., Costa et al. 2009), which at the rheological transition predicts a large reduction in the convective velocity and rapid melt–solid separation (Abe 1993). Hence somewhat coincidentally, previous models decrease the melt reservoir and outgas volatiles at a similar rate to geochemical fractional crystallisation models, even though the key ingredient to justify fractional crystallisation (i.e., melt–solid separation) is not included.

#### 4.4. Graphite and water precipitation

Reducing conditions may induce graphite or diamond precipitation (Hirschmann 2012; Takahashi et al. 2013; Keppler & Golabek 2019). The precipitation of graphite occurs if the CO fugacity of the atmosphere exceeds that defined by the graphite–carbon monoxide (CCO) buffer:



where  $K_{\text{eq}}$  as a function of temperature is provided by the JANAF database (Chase 1998). Equation 11 indicates that  $\log_{10} f\text{CO}$  in equilibrium with graphite decreases proportional to  $0.5 \log_{10} f\text{O}_2$  and increases with temperature. Thus, graphite precipitation is favoured under more reducing conditions and lower temperatures (Figure 13). For our cases at  $f\text{O}_2\text{s}$  of  $\Delta\text{IW}=0.5$  or more oxidised, graphite precipitation would not occur because  $f\text{CO}$  never exceeds that defined by the CCO buffer. This suggests it is unlikely that a terrestrial magma ocean was saturated in graphite at high melt fractions ( $> 30\%$ ). However, it may occur for most atmospheres as the surface cools below the temperature at which a surface lid forms around 1650 K (Sossi et al. 2020). At this stage, however, the atmosphere and man-

tle are not necessarily in equilibrium and the atmosphere can evolve as a near-closed system.

For a magma ocean more reduced than IW, the modelled cases at  $fO_2$  of  $\Delta IW = -2$  and  $C/H = 5$  show that graphite precipitation would occur in a cooling atmosphere, even accounting for the production of  $CH_4$  that buffers  $fCO$  (Figure 13). Specifically, higher initial C budgets result in higher  $fCO$ , where, for  $C/H = 5$ , the scenario with 10 oceans crosses the CCO buffer at  $\sim 2300$  K, while it does so at  $\sim 2000$  K for 5 oceans. As such, the quoted fugacities of carbon-bearing species for these two scenarios are upper limits. Cases at  $C/H = 1$  and  $\Delta IW = -2$  do not result in graphite saturation at any temperature, irrespective of the number of oceans, owing to the lower  $fCO$ .

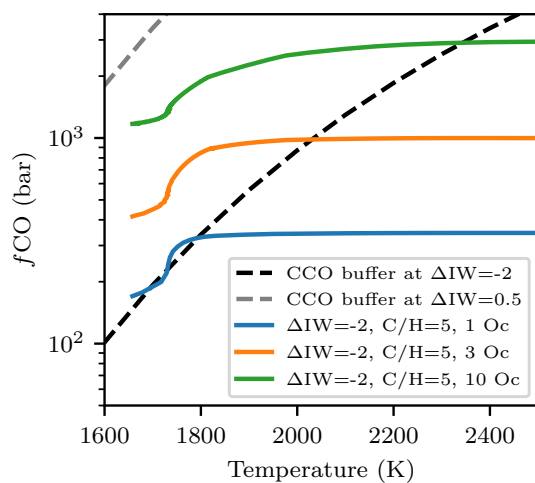
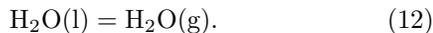


**Figure 13.** The fugacity of CO in equilibrium with graphite (Equation 11) assuming ideal gas behaviour as a function of temperature at  $\Delta IW = -2$  (dashed black line) and  $\Delta IW = 0.5$  (dashed grey line). All cases at  $\Delta IW = -2$  and  $C/H = 5$  (coloured lines) intercept the CCO buffer at  $\Delta IW = -2$ , indicating graphite precipitation. No other cases intercept the CCO buffer and are therefore not plotted.

A second important phase change can occur in cooling atmospheres, namely, that between liquid water and steam:



Its equilibrium constant as a function of temperature indicates that, at 1400 K,  $H_2O$  condenses at about 600 bar  $fH_2O$ . This phase transformation is neglected in our simulations primarily because these pressures and temperatures exceed the critical point of water, which is 650 K and 220 bar. Hence at 600 bar  $fH_2O$  the atmosphere is a supercritical fluid rather than an ideal gas as modelled herein. Moreover, the mixing of  $CO_2$  and  $H_2O$  is non-ideal, such that departures from ideal gas behaviour

are expected in these solutions (Duan et al. 1992; Frost & Wood 1997).

#### 4.5. Meteoritic degassing

Theoretical calculations (Schaefer & Fegley 2010) and outgassing experiments (Thompson et al. 2021) predict the composition of gases evolved from the degassing of meteoritic materials, some of which may be representative of planetary building blocks. By examining equilibrium between gas and condensed phases, thermodynamic models find that  $H_2$  and  $CO$  gases form from reduced chondrites (such as EH) at high temperature (Schaefer & Fegley 2010). Only for the most oxidising materials (CI chondritic composition) is  $H_2O$  predicted to be a major constituent of the gas mixture. Since water is only an important gaseous species during degassing of one particular class of chondrite calls into question the applicability of steam atmospheres to the evolution of terrestrial planets at large.

Although instructive, directly correlating gases produced from meteorites to the composition of planetary atmospheres is complicated for several reasons. Meteorites are imperfect analogues of the material that went on to form the terrestrial planets (Sossi 2021), particularly as regards volatile elements due to the ubiquitous alteration processes occurring on their parent body (Brearley 2006) as well as thermal metamorphism and the likelihood that planetesimals are already differentiated when they accrete. More importantly, the likely presence of a deep magma ocean during and immediately post-accretion would have modified the budgets of elements available to degas at the planetary surface (e.g., Grewal et al. 2020; Dalou et al. 2019). As shown in our work, equilibrium reactions between silicate melt and volatiles in the gas phase influence the partitioning of gas species between the atmosphere and magma ocean according to their solubility. Furthermore, some volatiles (including H and C) may be permanently sequestered into an iron core due to their siderophile nature (e.g., Tagawa et al. 2021).

Therefore, connecting gas mixtures to atmospheric composition necessitates an assumption that the starting bulk composition—usually derived from chondrites—adequately captures elemental abundances in the atmosphere during and after the magma ocean phase. This assumes that volatiles did not experience significant partitioning due to magma ocean and core formation processes, and that atmosphere formation proceeds by the breakdown of solid mineral assemblages (i.e., degassing occurs subsolidus). Solid bodies cannot efficiently replenish surface material from deeper regions, whereas for molten bodies the entire melt mass can communicate

with the atmosphere over a short timescale. Alternatively, partitioning can be permitted under the assumption that ongoing impact-induced outgassing of chondritic materials after a surface lid forms (e.g. in a late-veener scenario or during the late-heavy bombardment) is sufficient to displace or dilute any previously equilibrated atmosphere (Zahnle et al. 2020).

Extraction of volatiles to solids in the core or mantle locks them away from outgassing to the atmosphere over a short timescale, and perhaps indefinitely. By contrast, volatiles partitioned in melt are readily available to outgas during mantle crystallisation as long as the interior and atmosphere remain in thermodynamic communication (e.g., for fractional crystallisation). Accounting for thermodynamic equilibrium with silicate melt, we demonstrate that the earliest atmosphere evolves in both mass and composition during magma ocean cooling. An atmosphere can transition from dominantly CO-rich (‘reducing’) to H<sub>2</sub>O-rich (‘oxidising’) due to solubility and redox reactions as the magma ocean cools (Figure 12). Therefore, the solubility of volatiles in silicate melt prevents drawing a simple connection between the composition of planetary building blocks and the earliest atmospheres of terrestrial planets.

## 5. SUMMARY AND CONCLUSIONS

The investigation of catastrophic outgassing of CO<sub>2</sub> and H<sub>2</sub>O from terrestrial magma oceans—as well as their influence on the nature of early atmospheres around rocky planets—was originally motivated by the degassing of hydrated minerals and oxidised chondritic materials. However, for redox conditions appropriate for the early Earth, we find that CO is usually the dominant atmospheric species during the early molten stage where the melt fraction is greater than 30% (Figure 12). This is due to the relatively high solubility of hydrogen species (H<sub>2</sub>O) compared to carbon species (CO<sub>2</sub>), as well as redox reactions that govern CO–CO<sub>2</sub>, H<sub>2</sub>–H<sub>2</sub>O, and CO<sub>2</sub>–H<sub>2</sub>–CH<sub>4</sub> equilibria. Only when C/H by weight is small (C/H < 0.1) and the H budget large (>6 oceans) can H species constitute more than 50% of the atmosphere, with H<sub>2</sub> and H<sub>2</sub>O in approximately equal abundance (Figure 4). For more oxidising conditions, early atmospheres are dominated by CO<sub>2</sub> with H<sub>2</sub>O a minor species (Figure 8).

For the late molten stage (< 30% melt), more H is retained (relative to the total budget) for smaller H budgets, larger C/H, and more oxidising conditions (Figure 12). At this stage, continued outgassing driven by dissolution equilibrium requires that the surface remains molten and a persistent lid does not form; this requirement can be satisfied if a magma ocean undergoes

fractional crystallisation. However, for magma oceans that freeze more quickly by equilibrium crystallisation, formation of a surface lid around 30% melt can prevent subsequent outgassing of highly soluble volatiles such as H<sub>2</sub>O. This would leave the atmosphere as carbon/CO dominated by stifling the formation of a steam atmosphere. Methane only forms for reduced conditions ( $\Delta IW \lesssim 0.5$ ) when pressures are sufficiently high or temperatures sufficiently low; otherwise CH<sub>4</sub> is absent. Graphite precipitation from the atmosphere during magma ocean cooling is expected only for very high C budgets (higher than those anticipated for Earth) and for  $\Delta IW \lesssim 0.5$ . Nevertheless, for all cases, graphite in the atmosphere may precipitate with continued cooling.

We find that the majority of H could remain in planetary mantles and outgas over geological timescales, potentially impacting the timescale for water ocean formation and the ability to desiccate planets. Furthermore, hydrogen species would only play a minor role in determining atmospheric opacity or modulating atmospheric escape; rather, the behaviour of carbon species is dominant. The style of magma ocean crystallisation—fractional or equilibrium—is therefore a fundamental variable in determining the composition and mass of early atmospheres and the efficiency of volatile delivery to the planetary atmosphere and surface. Ultimately, the high solubility of H<sub>2</sub>O in magma oceans may enable its safe storage during the tumultuous phase of planet formation.

## 6. DATA AVAILABILITY

All of the data generated as part of this study can be obtained by contacting Dan J. Bower.

DJB acknowledges Swiss National Science Foundation (SNSF) Ambizione Grant 173992. KH is supported by the European Research Council via Consolidator Grant ERC-2017-CoG-771620-EXOKLEIN. PAS acknowledges Swiss National Science Foundation (SNSF) Ambizione Grant 180025. PS acknowledges financial support from the Swiss University Conference and the Swiss Council of Federal Institutes of Technology through the Platform for Advanced Scientific Computing (PASC) program. This research was partly inspired by discussions and interactions within the framework of the National Center for Competence in Research (NCCR) PlanetS supported by the SNSF. The calculations were performed on UBELIX (<http://www.id.unibe.ch/hpc>), the HPC cluster at the University of Bern. We thank S. Grimm and D. Kitzmann for computing Rosseland mean opacities, and A. Wolf, M. Tian, and T. Lichtenberg for discussions and feedback on the manuscript. Two anonymous referees provided comments that further enhanced the manuscript.

*Software:* Simulating Planetary Interior Dynamics with Extreme Rheology (SPIDER) (Bower et al. 2018, 2019) is open source and hosted at <https://bitbucket.org/djbower/spider>.

## APPENDIX

## A. OPACITIES

We computed Rosseland mean opacities at 1 bar between 1700 K and 2700 K for H<sub>2</sub>O, H<sub>2</sub>, CO<sub>2</sub>, CO, and CH<sub>4</sub> using Helios-k (Grimm et al. 2021; Grimm & Heng 2015). The opacity (Rosseland mean mass absorption coefficient) for H<sub>2</sub>O using the full BT2 list (Barber et al. 2006) is  $1.5 \times 10^{-2}$  m<sup>2</sup>/kg at 1700 K and  $5.0 \times 10^{-4}$  m<sup>2</sup>/kg at 2700 K; the opacity at 1800 K compares favourably with  $10^{-2}$  m<sup>2</sup>/kg which has been used extensively in previous magma ocean studies. For simplicity we also adopt a constant value (i.e., independent of temperature) of  $10^{-2}$  m<sup>2</sup>/kg. The opacity of H<sub>2</sub> is determined by collision-induced absorption (CIA) and using HITRAN (Karman et al. 2019; Abel et al. 2011) it is essentially constant ( $5 \times 10^{-5}$  m<sup>2</sup>/kg) from 2700 K to 1700 K.

For CO<sub>2</sub>, HITEMP (Rothman et al. 2010) provided the line list and we determined an opacity of  $1.5 \times 10^{-4}$  m<sup>2</sup>/kg at 1700 K and  $3 \times 10^{-5}$  m<sup>2</sup>/kg at 2700 K. Hence the CO<sub>2</sub> opacity at 1700 K is compatible with  $10^{-4}$  m<sup>2</sup>/kg, which is the lowest opacity considered for CO<sub>2</sub> in previous magma ocean models. To be consistent with our selection of the H<sub>2</sub>O opacity around 1800 K, we similarly adopt a constant CO<sub>2</sub> opacity of  $10^{-4}$  m<sup>2</sup>/kg. For CO we determined an opacity of  $1.2 \times 10^{-5}$  m<sup>2</sup>/kg at 1700 K and  $3 \times 10^{-6}$  m<sup>2</sup>/kg at 2700 K using HITEMP (Li et al. 2015a). Again, we selected an opacity of  $10^{-5}$  m<sup>2</sup>/kg based on the value at 1800 K. We computed a CH<sub>4</sub> opacity of  $10^{-2}$  m<sup>2</sup>/kg at 1800 K based on the line lists of Yurchenko et al. (2013); Yurchenko & Tennyson (2014). The opacities of species at 1 bar are reference opacities that are used to compute a pressure-dependent opacity (Equation A22, Abe & Matsui 1985).

## B. MELT–SOLID SEPARATION

The fluxes to describe energy transport in a planetary mantle (which is molten, partially molten, or solid) are described in detail in Bower et al. (2018); Abe (1995). However, we recap the physics underpinning melt–solid separation due to its importance for determining whether a mantle undergoes fractional or equilibrium crystallisation. At high melt fraction, the settling or flotation of crystals within a magma ocean is determined by Stokes’ law:

$$u_m - u_s = \frac{2a^2g(\rho_m - \rho_s)}{9\eta_m}, \quad (\text{B1})$$

where  $u$  is velocity (positive radially outwards),  $a$  crystal size,  $g$  gravity (negative),  $\rho$  density,  $\eta$  viscosity, and subscripts  $m$  and  $s$  denote melt and solid, respectively. Interaction amongst crystals is not considered and therefore free settling or flotation of crystals is an upper limit on the efficiency of melt–solid separation at high melt fraction. At low melt fraction, separation occurs via Darcy flow:

$$u_m - u_s = \frac{k_p g(\rho_m - \rho_s)}{\phi_p \eta_m}, \quad (\text{B2})$$

where  $k_p$  is permeability and  $\phi_p$  porosity (synonymous with the volume fraction of melt). The Rumpf–Gupte permeability law is appropriate at intermediate porosity (Rumpf & Gupte 1971)

$$k_{rg} = \frac{a^2 \phi_p^{5.5}}{1.4}, \quad (\text{B3})$$

and the Blake–Kozeny–Carman permeability law at low porosity:

$$k_{bkc} = \frac{a^2 \phi_p^3}{1000(1 - \phi_p)^2}. \quad (\text{B4})$$

The constants in these permeability laws are constrained by experiments (see McKenzie 1984; Abe 1995, for discussion). The flow laws can be represented by a single description (Abe 1995):

$$u_m - u_s = \frac{a^2 g(\rho_m - \rho_s)}{\eta_m} f, \quad (\text{B5})$$

$$f = \begin{cases} \frac{2}{9} & \text{for } 0.77 \leq \phi_p, \\ \frac{k_{rg}}{a^2 \phi_p} & \text{for } 0.08 < \phi_p < 0.77, \\ \frac{k_{bkc}}{a^2 \phi_p} & \text{for } \phi_p \leq 0.08, \end{cases} \quad (\text{B6a})$$

$$f = \begin{cases} \frac{2}{9} & \text{for } 0.77 \leq \phi_p, \\ \frac{k_{rg}}{a^2 \phi_p} & \text{for } 0.08 < \phi_p < 0.77, \\ \frac{k_{bkc}}{a^2 \phi_p} & \text{for } \phi_p \leq 0.08, \end{cases} \quad (\text{B6b})$$

$$f = \begin{cases} \frac{2}{9} & \text{for } 0.77 \leq \phi_p, \\ \frac{k_{rg}}{a^2 \phi_p} & \text{for } 0.08 < \phi_p < 0.77, \\ \frac{k_{bkc}}{a^2 \phi_p} & \text{for } \phi_p \leq 0.08, \end{cases} \quad (\text{B6c})$$

where the range of applicability of each flow law ensures that  $f$  is a continuous function of porosity. Through consideration of the local barycentric velocity, the mass flux of melt is:

$$J_m = \rho \phi(1 - \phi)(u_m - u_s), \quad (\text{B7})$$

where  $\phi$  is melt fraction (the mass fraction of melt). Equation B7 naturally satisfies the requirement that  $J_m = 0$  for  $\phi = 0$  and  $\phi = 1$ . The energy flux of melt–solid separation is therefore:

$$F_{\text{grav}} = J_m T_{\text{fus}} \Delta S_{\text{fus}}, \quad (\text{B8})$$

where  $T_{\text{fus}}$  is the temperature at 50% melt fraction and  $\Delta S_{\text{fus}}$  is the entropy of fusion, both of which are functions of pressure according to the melting curves. Equation B5 reveals the common factors appearing in all of the flow laws and emphasises the importance of crystal size due to its squared dependence: larger crystals enhance melt–solid separation. Since we consider a single component mantle ( $\text{MgSiO}_3$ ), everywhere  $\rho_m - \rho_s < 0$  and hence crystals always sink and melt always drains upwards to the surface.

## C. MAGMA OCEAN AND ATMOSPHERE EQUILIBRIUM

### C.1. Volatile mass balance and evolution

We extended Bower et al. (2019) to express the mass balance for a volatile  $v$  in a chemically reactive environment with atmospheric escape:

$$\begin{aligned} X_v k_v M^s + X_v M^l + 4\pi R_p^2 \left( \frac{\mu_v}{\bar{\mu}} \right) \frac{p_v}{|g|} + m_v^e + \sum_{w=1}^r m_v^w \\ = X_v^0 M^m, \end{aligned} \quad (\text{C9})$$

where:

- $X_v$  volatile abundance in the pure melt
- $k_v$  distribution coefficient between solid and melt
- $M^s$  mantle mass of solid
- $M^l$  mantle mass of melt
- $M^m = M^s + M^l$  is total mantle mass, which is constant
- $R_p$  planetary surface radius
- $g$  surface gravity
- $\mu_v$  molar mass of the volatile
- $\bar{\mu}$  mean molar mass of the atmosphere
- $p_v$  surface partial pressure of the volatile
- $X_v^0$  initial total volatile abundance relative to the total mantle mass.

A solubility law relates the volatile concentration in the melt ( $X_v$ ) to the partial pressure of the volatile in the atmosphere ( $p_v$ ). The first three terms on the left hand side of Equation C9 represent the mass of the volatile stored in the solid mantle, the molten mantle, and the atmosphere. The final two terms on the LHS are fictitious reservoirs used to account for mass loss due to

escape ( $m_v^e$ , Appendix C.2), and mass transfer due to participation of this volatile in reaction  $w$  ( $m_v^w$ , Appendix C.3). The time derivative of Equation C9 derives the evolution equation (cf., Equation A4, Bower et al. 2019):

$$\begin{aligned} \frac{dX_v}{dt} (k_v M^m + (1 - k_v) M^l) + X_v (1 - k_v) \frac{dM^l}{dt} \\ + \frac{4\pi R_p^2 \mu_v}{|g|} \left[ \frac{1}{\bar{\mu}} \frac{dp_v}{dt} - \frac{p_v}{\bar{\mu}^2} \sum_{w=1}^n \frac{\mu_w}{P_s} \left( \frac{dp_w}{dt} - \frac{p_w}{P_s} \frac{dP_s}{dt} \right) \right] \\ + \frac{dm_v^e}{dt} + \sum_{w=1}^r \frac{dm_v^w}{dt} = 0, \end{aligned} \quad (\text{C10})$$

where  $P_s$  is the total surface pressure, which is equal to the summation of the partial pressures of all volatiles according to Dalton’s Law. The derivative of  $X_v$  with respect to  $t$  can be determined from the solubility law relevant for volatile  $v$ , which for power-law solubility (Equation 1) is:

$$\frac{dX_v}{dt} = \frac{dX_v}{dp_v} \frac{dp_v}{dt} = \left( \frac{\alpha_v p_v^{1/\beta_v - 1}}{\beta_v} \right) \frac{dp_v}{dt}. \quad (\text{C11})$$

Similarly,  $X_v$  can be eliminated from Equation C10 using the solubility law. This results in a system of non-linear equations that can be solved simultaneously to determine  $dp_v/dt$  for each volatile  $v$ . Solving for  $dp_v/dt$  rather than  $dX_v/dt$  enables us to treat the case of zero solubility. Oxygen fugacity  $f_{\text{O}_2}$  (Equation 7) depends on surface temperature so oxygen is not explicitly tracked by mass balance as with the other volatiles.

### C.2. Mass loss due to atmospheric escape

The escape flux of  $\text{H}_2$  (Equation 9) is used to determine a mass loss rate of  $\text{H}_2$  (e.g., Katyal et al. 2020):

$$\frac{dm_{\text{H}_2}^e}{dt} = 4\pi R_p^2 \phi_{\text{H}_2} \mu_{\text{H}_2}. \quad (\text{C12})$$

The loss rate depends on the time-dependent volume mixing flux of  $\text{H}_2$  through  $\phi_{\text{H}_2}$ . In turn, the volume mixing ratio of  $\text{H}_2$  is computed from the partial pressure of  $\text{H}_2$  and the total surface pressure. In the present work, the mass loss rate for volatiles other than  $\text{H}_2$  is set to zero.

### C.3. Mass exchange due to chemical reactions

During the magma ocean stage, the silicate melt and overlying atmosphere can accommodate mass exchange via chemical reactions. We consider a general reaction with two reactants (A, B) and two products (C, D):



where  $a$ ,  $b$ ,  $c$ , and  $d$  are stoichiometric coefficients. The reaction quotient  $Q$  is a function of time  $t$ :

$$Q(t) = \frac{\{C\}^c \{D\}^d}{\{A\}^a \{B\}^b} \doteq \frac{Q_p(t)}{Q_r(t)}, \quad (\text{C14})$$

where curly brackets  $\{\}$  denote the activity of the species and the activity of a gas is its fugacity divided by a reference pressure. At chemical equilibrium, the reaction quotient is equal to the equilibrium constant  $K$ , which is a function of temperature. An appropriate temperature is that of the magma ocean–atmosphere interface, hence:

$$\frac{\{C\}^c \{D\}^d}{\{A\}^a \{B\}^b} - K(T) = 0. \quad (\text{C15})$$

The reaction in Equation C13 can also be expressed in terms of a mass balance of reactants and products:

$$m_A + m_B \rightleftharpoons m_C + m_D. \quad (\text{C16})$$

This is because the fractional change of moles corresponds to the fractional change of mass, so correlating terms in Equation C13 and C16:

$$m_B = \left( \frac{b\mu_B}{a\mu_A} \right) m_A, \quad m_C = \left( \frac{c\mu_C}{a\mu_A} \right) m_A, \quad \text{etc.} \quad (\text{C17})$$

where  $\mu$  is the molar mass. It is convenient in Equation C17 to express the mass of the reactants and products using the mass of the first reactant ( $m_A$ ) multiplied by a constant factor that depends only on molar masses and reaction stoichiometry; mathematically this choice is arbitrary and another mass could equally be used. Hence, each chemical reaction introduces a single unknown ‘reaction mass’ ( $m_A$ ) and one equation (Equation C15) to the complete system of equations that we solve. The functional dependencies of all quantities in Equation C15 are known, since we assume ideal gas behaviour to connect gas activities to volatile partial pressures and the functional dependence of the equilibrium constant on temperature  $T$  is documented in thermochemical tables (Chase 1998).

Evolution equations of Equations C15 and C17 are necessary to timestep the model. The time derivatives of the reactant and product masses are trivial to compute since stoichiometric coefficients and molar masses are constant. For example (c.f., Equation C17):

$$\frac{dm_B}{dt} = \left( \frac{b\mu_B}{a\mu_A} \right) \frac{dm_A}{dt}, \quad (\text{C18})$$

and the time derivative of the reactant masses ( $m_C$ ,  $m_D$ ) can be similarly computed. The time derivative of the equilibrium condition (Equation C15) is:

$$\frac{1}{Q_r} \frac{dQ_p}{dt} - \frac{Q_p}{Q_r^2} \frac{dQ_r}{dt} - \frac{dK}{dT} \frac{dT}{dt} = 0, \quad (\text{C19})$$

where the reaction quotient numerator  $Q_p = \{C\}^c \{D\}^d$  and denominator  $Q_r = \{A\}^a \{B\}^b$  depend on the volatile partial pressures and reaction stoichiometry. The equilibrium constant  $K$  depends only on temperature  $T$  (Equations 4 and 5) and therefore  $dK/dT$  is straightforward to evaluate. The code also solves for  $dT/dt$  in the mantle at each staggered mesh point, although only the change of surface temperature is required since this temperature defines the interface of the magma ocean and atmosphere.

Hence to include reactions in the time stepper, Equation C19 constitutes an extra equation per reaction that must be satisfied, where the extra unknowns we solve for are the change of reaction mass for each reaction ( $dm_A/dt$ ). Equation C18 relates the change of reaction mass for reactant  $B$  and products  $C$  and  $D$  to the solution quantity ( $dm_A/dt$ ). For each volatile, we can thus evaluate the total rate-of-change of its mass due to all reactions that it participates in; this is the final term on the left-hand side of Equation C10.

#### C.4. Initial volatile abundances

For the initial condition, we solve for the abundance of each volatile in the melt using a set of coupled equations consisting of all the volatile mass balances (Equation C9) and  $r$  chemical reactions (Equation C15). To do this, estimates of the initial total volatile abundances  $X_v^{0,\text{est}}$  are prescribed and the initial atmospheric escape masses are set to zero ( $m_v^e = 0$ ). We solve for the partial pressure of each volatile in the atmosphere and the reaction masses, the later of which are likely to be non-zero. Hence it is convenient—although formally not necessary—to offset the estimates of the initial total volatile abundances ( $X_v^{0,\text{est}}$ ) using the solved reaction masses to enforce that the initial total volatile abundances ( $X_v^0$ ) adhere to chemical equilibrium constraints with zero reaction mass:

$$X_v^0 = X_v^{0,\text{est}} - \frac{1}{M^m} \sum_w^r m_v^w. \quad (\text{C20})$$

Hence the reaction masses are zero by definition for the initial condition and can increase or decrease during the time integration.

### C.5. Alternative using thermodynamic components

The system of volatiles we consider can be represented by two components: C and H<sub>2</sub>, where we recall that oxygen is not explicitly tracked. Hence an alternative approach to solving the mass balance for each volatile is to instead solve for the total abundance of C and H<sub>2</sub> moles. Conservation laws for C and H<sub>2</sub> abundances can be derived by converting the relevant volatile mass balances to C or H<sub>2</sub> moles and then summing. Without chemical reactions, conserving species mass or abundance is the same, because there is no exchange of material between species. With reactions, one can either continue to track species mass by accounting for mass exchange by reactions (as we choose to do), or alternatively one can instead track the abundance of components. Considering species mass allows one to retain the familiar mass formulation derived without reactions, but at the expense of more equations (e.g., 5 volatile species plus 3 reactions). By contrast, considering components reduces the number of equations (e.g., 2 components plus 3 reactions), but requires a departure from the traditional species mass balance approach. Ultimately, both approaches are valid and equivalent and will likely find utility in different applications.

### C.6. Simplified mass balance and interior depletion

The partitioning of volatiles between a fully molten magma ocean and atmosphere can be analysed using a reduced form of the volatile mass balance (Equation C9). This aids the interpretation of the results—notably demonstrating their universality—as well as providing analytical expressions and scaling relations. We consider the mass balance for a single volatile that is only partitioned between the melt and atmosphere. However, we retain the mean molar mass of the atmosphere  $\bar{\mu}$  to provide insight when the atmosphere is dominated by the presence of another (or mixture) of volatiles that are less soluble than the volatile under consideration. Following Equation C9:

$$X_v M^l + 4\pi R_p^2 \left( \frac{\mu_v}{\bar{\mu}} \right) \frac{p_v}{|g|} = X_v^0 M^m. \quad (\text{C21})$$

For power-law solubility (Equation 1):

$$\frac{\phi_g}{C} X_v + X_v^{\beta_v} = \frac{X_v^0}{C}, \quad (\text{C22})$$

where  $\phi_g = M^l/M^m$  is the global melt fraction and

$$C = \frac{4\pi R_p^2 \mu_v \alpha_v^{-\beta_v}}{M^m \bar{\mu} |g|}. \quad (\text{C23})$$

For a single species ( $\bar{\mu} = \mu_v$ ), an Earth-sized mantle, and values of  $\alpha_v$  and  $\beta_v$  from the peridotite solubility law (Table 1), the coefficient  $C \approx 17/4$ .

#### C.6.1. Volatile depletion for $\beta_v = 2$

For the peridotite solubility law (as well as other laws),  $\beta_v = 2$  and Equation C22 is a quadratic equation that can be solved for the volatile abundance in the melt:

$$X_v = \frac{-\phi_g}{2C} + \frac{1}{2} \sqrt{\frac{\phi_g^2}{C^2} + \frac{4X_v^0}{C}}. \quad (\text{C24})$$

Hence comparing to Equation C22, the scaled volatile mass in the liquid is:

$$m_v^l = \frac{-\phi_g^2}{2C^2} + \frac{\phi_g}{2C} \sqrt{\frac{\phi_g^2}{C^2} + \frac{4X_v^0}{C}}, \quad (\text{C25})$$

the scaled volatile mass in the atmosphere is:

$$m_v^a = \frac{X_v^0}{C} + \frac{\phi_g^2}{2C^2} - \frac{\phi_g}{2C} \sqrt{\frac{\phi_g^2}{C^2} + \frac{4X_v^0}{C}}, \quad (\text{C26})$$

and the scaled total volatile mass is:

$$m_v^t = \frac{X_v^0}{C}. \quad (\text{C27})$$

Therefore, the volatile depletion  $\mathcal{D}$  expressed as a fraction relative to the total volatile mass is:

$$\mathcal{D} = 1 - \frac{m_v^l}{m_v^t} = \frac{m_v^a}{m_v^t} = 1 + \frac{\phi_g^2}{2CX_v^0} - \frac{\phi_g}{2X_v^0} \sqrt{\frac{\phi_g^2}{C^2} + \frac{4X_v^0}{C}}. \quad (\text{C28})$$

Taking the derivative of Equation C28 with respect to the initial volatile abundance  $X_v^0$ , we obtain:

$$\frac{\partial \mathcal{D}}{\partial X_v^0} = \frac{\phi_g \left( -\phi_g \sqrt{\phi_g^2 + 4CX_v^0} + \phi_g^2 + 2CX_v^0 \right)}{2(X_v^0)^2 C \sqrt{\phi_g^2 + 4X_v^0 C}}. \quad (\text{C29})$$

All variables must be positive to be physically meaningful. The denominator is clearly always positive and the numerator is also positive since the following condition is always satisfied:

$$\phi_g^2 + 2CX_v^0 > \phi_g \sqrt{\phi_g^2 + 4CX_v^0}. \quad (\text{C30})$$

Therefore:

$$\frac{\partial \mathcal{D}}{\partial X_v^0} > 0. \quad (\text{C31})$$

Hence at a given melt fraction  $\phi_g$ , the relative depletion of the interior increases with the initial volatile abundance  $X_v^0$  (Figure 3).

C.6.2. Volatile depletion for  $\beta_v = 1$ 

For a volatile that obeys Henrian solubility behaviour ( $\beta_v = 1$ ), similar to Appendix C.6.1 we can write:

$$X_v = \frac{X_v^0}{C + \phi_g}, \quad m_v^l = \frac{\phi_g X_v^0}{C(C + \phi_g)}, \quad m_v^a = \frac{X_v^0}{C + \phi_g}. \quad (\text{C32})$$

Hence the interior depletion  $\mathcal{D}$  is:

$$\mathcal{D} = \frac{C}{C + \phi_g}, \quad \frac{\partial \mathcal{D}}{\partial X_v^0} = 0. \quad (\text{C33})$$

Notably, interior depletion is independent of the initial volatile abundance  $X_v^0$  when  $\beta_v = 1$ .

## D. OXYGEN FUGACITY AND ATMOSPHERE SPECIATION

Figure 4 shows the atmospheric composition at an oxygen fugacity of  $\Delta IW=0.5$ . The following figures show the same at  $\Delta IW=-2$  (Figure 14),  $\Delta IW=2$  (Figure 15), and  $\Delta IW=4$  (Figure 16).

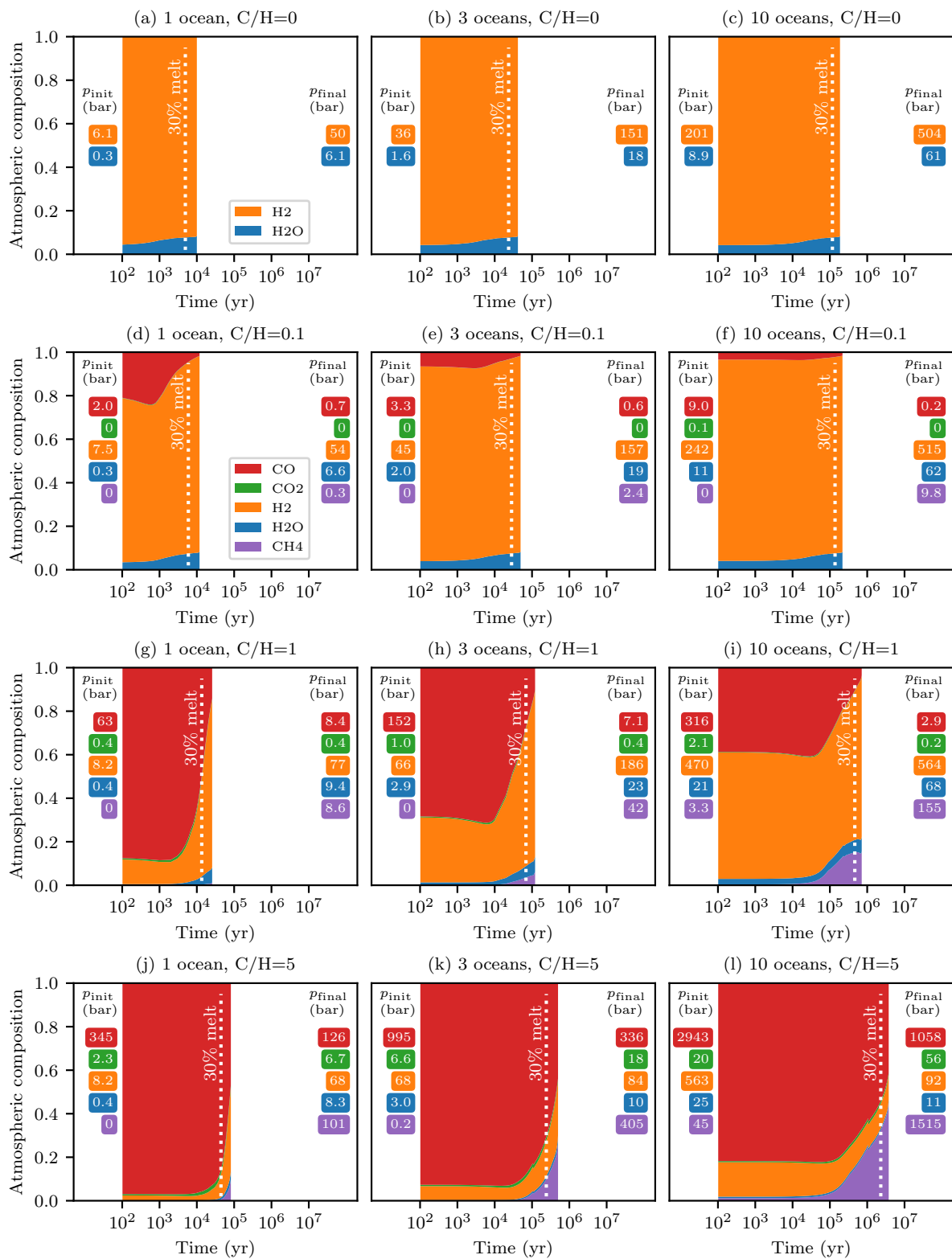


**Figure 14.** Atmospheric composition during magma ocean outgassing at  $fO_2$  of  $\Delta IW = -2$ . See Figure 4 caption.

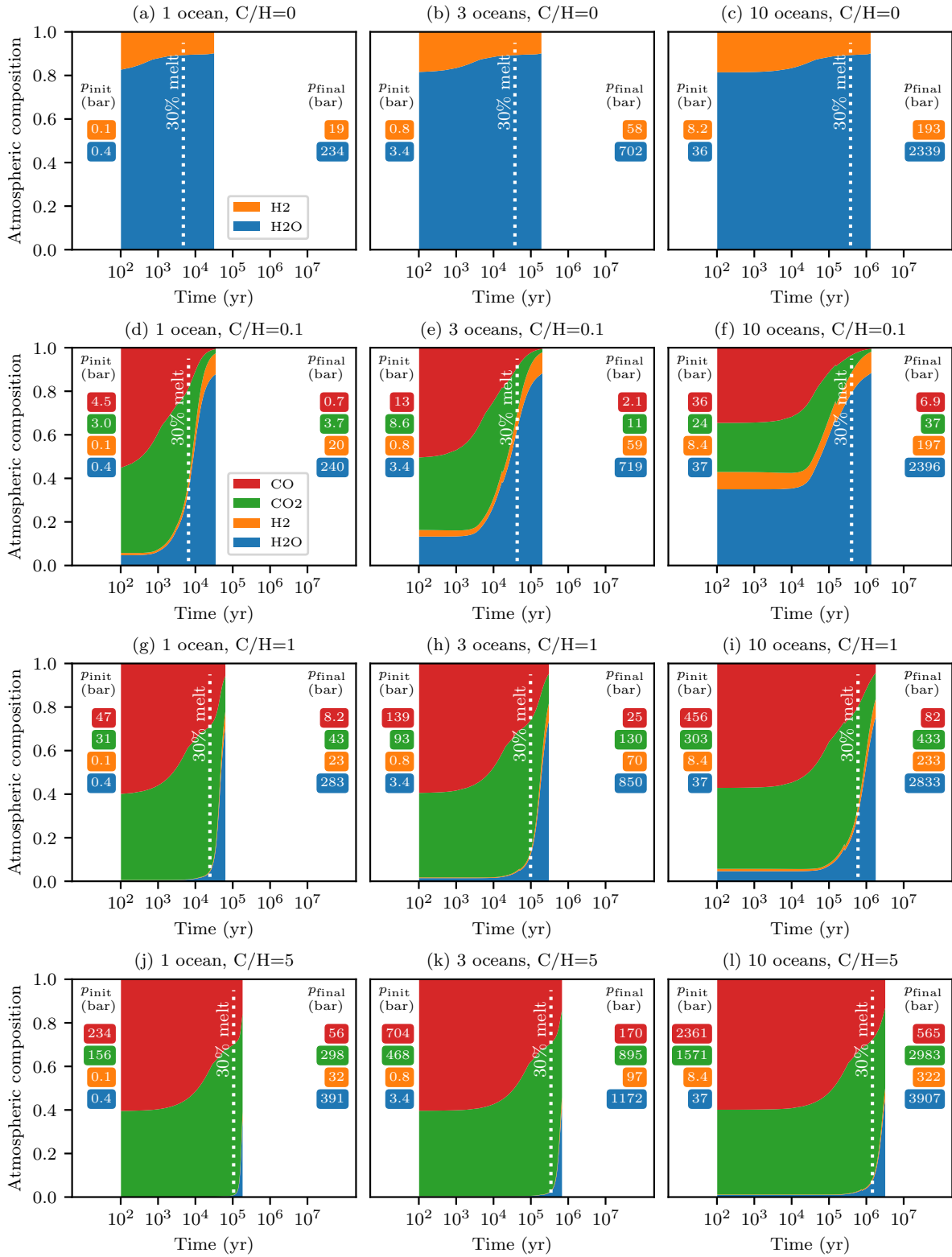


**Figure 15.** Atmospheric composition during magma ocean outgassing at  $f_{O_2}$  of  $\Delta IW=2$ . See Figure 4 caption.

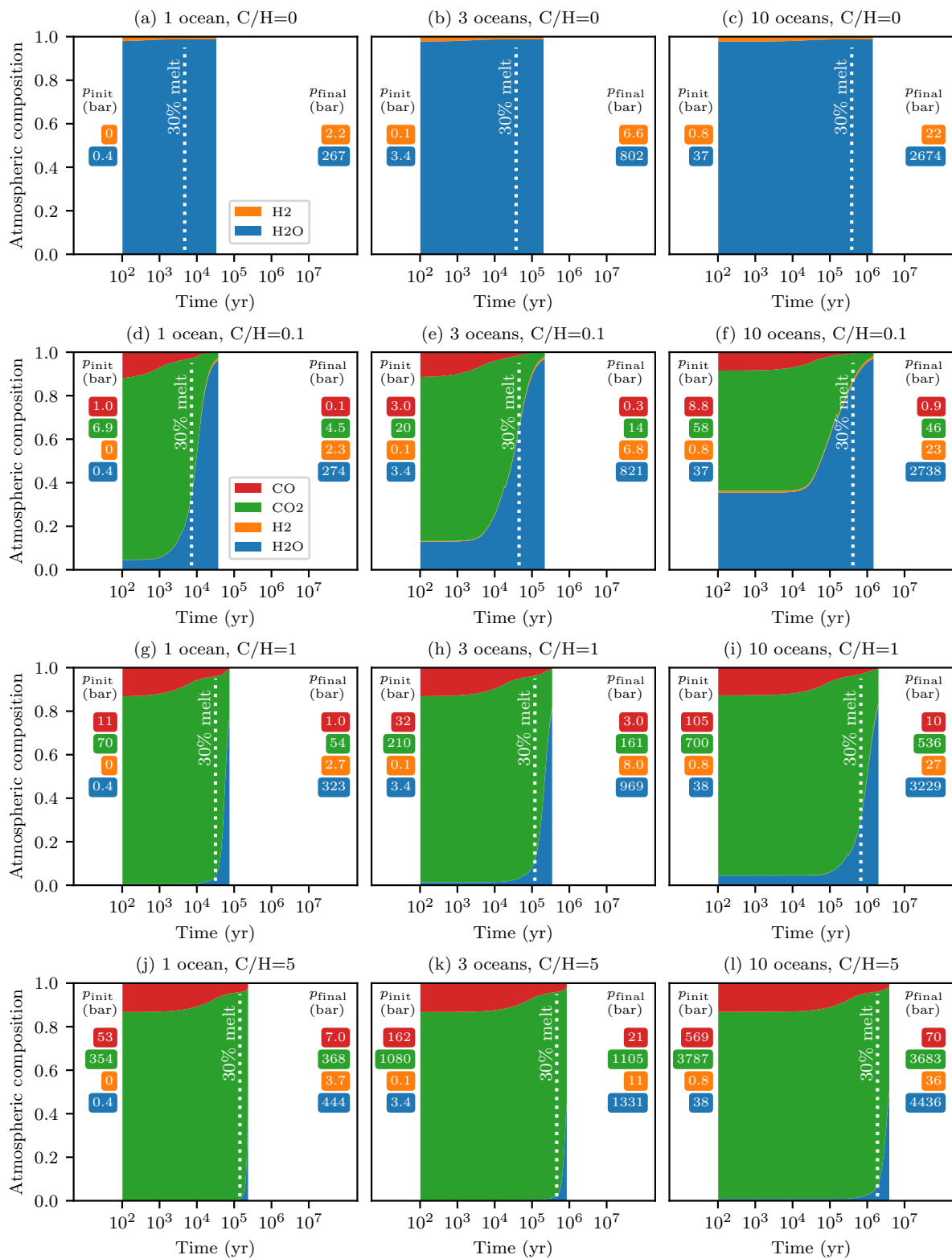


**Figure 16.** Atmospheric composition during magma ocean outgassing at  $f_{O_2}$  of  $\Delta IW=4$ . See Figure 4 caption.

## REFERENCES

- Abe, Y. 1993, *Thermal Evolution and Chemical Differentiation of the Terrestrial Magma Ocean*, ed. E. Takahashi, R. Jeanloz, & D. Rubie, Vol. 74 (AGU, Washington, D.C.), 41–54, doi: <https://doi.org/10.1029/GM074p0041>
- . 1995, in *The Earth's Central Part: Its Structure and Dynamics*, ed. T. Yukutake (Terra Sci. Pub. Com., Tokyo), 215–230. <https://www.terrapub.co.jp/e-library/ecp/pdf/EC0215.PDF>
- Abe, Y., & Matsui, T. 1985, *JGRB*, 90, C545, doi: <https://doi.org/10.1029/JB090iS02p0C545>
- Abel, M., Frommhold, L., Li, X., & Hunt, K. L. C. 2011, *JPCA*, 115, 6805, doi: <https://doi.org/10.1021/jp109441f>
- Andrault, D., Bolfan-Casanova, N., Nigro, G. L., et al. 2011, *E&PSL*, 304, 251, doi: <https://doi.org/10.1016/j.epsl.2011.02.006>
- Andrault, D., Monteux, J., Bars, M. L., & Samuel, H. 2016, *E&PSL*, 443, 195, doi: <https://doi.org/10.1016/j.epsl.2016.03.020>
- Ardia, P., Hirschmann, M., Withers, A., & Stanley, B. 2013, *GeCoA*, 114, 52, doi: <https://doi.org/10.1016/j.gca.2013.03.028>
- Armstrong, K., Frost, D. J., McCammon, C. A., Rubie, D. C., & Boffa Ballaran, T. 2019, *Sci*, 365, 903, doi: <https://doi.org/10.1126/science.aax8376>
- Barber, R. J., Tennyson, J., Harris, G. J., & Tolchenov, R. N. 2006, *MNRAS*, 368, 1087, doi: <https://doi.org/10.1111/j.1365-2966.2006.10184.x>
- Barth, P., Carone, L., Barnes, R., et al. 2021, *AsBio*, doi: <https://doi.org/10.1089/ast.2020.2277>
- Benedikt, M., Scherf, M., Lammer, H., et al. 2020, *Icarus*, 347, 113772, doi: <https://doi.org/10.1016/j.icarus.2020.113772>
- Berndt, J., Liebske, C., Holtz, F., et al. 2002, *AmMin*, 87, 1717, doi: <https://doi.org/10.2138/am-2002-11-1222>
- Bonati, I., Lichtenberg, T., Bower, D. J., Timpe, M., & Quanz, S. 2019, *A&A*, 621, doi: <https://doi.org/10.1051/0004-6361/201833158>
- Bower, D. J., Kitzmann, D., Wolf, A. S., et al. 2019, *A&A*, 631, doi: <https://doi.org/10.1051/0004-6361/201935710>
- Bower, D. J., Sanan, P., & Wolf, A. S. 2018, *PEPI*, 274, 49, doi: <https://doi.org/10.1016/j.pepi.2017.11.004>
- Brearley, A. J. 2006, *The Action of Water*, ed. D. S. Lauretta & H. Y. McSween (University of Arizona Press), 587–624
- Caracas, R., Hirose, K., Nomura, R., & Ballmer, M. D. 2019, *E&PSL*, 516, 202, doi: <https://doi.org/10.1016/j.epsl.2019.03.031>
- Charnoz, S., Sossi, P. A., Lee, Y.-N., et al. 2021, *Icarus*, 364, 114451, doi: <https://doi.org/10.1016/j.icarus.2021.114451>
- Chase, M. 1998, *NIST-JANAF Thermochemical Tables*, 4th Edition (American Institute of Physics), doi: <https://doi.org/10.18434/T42S31>
- Corgne, A., Wood, B. J., & Fei, Y. 2008, *GeCoA*, 72, 2409, doi: <https://doi.org/10.1016/j.gca.2008.03.001>
- Costa, A., Caricchi, L., & Bagdassarov, N. 2009, *GGG*, 10, doi: <https://doi.org/10.1029/2008GC002138>
- Dalou, C., Hirschmann, M. M., Jacobsen, S. D., & Le Losq, C. 2019, *GeCoA*, 265, 32, doi: <https://doi.org/10.1016/j.gca.2019.08.029>
- Dasgupta, R. 2013, *RvMG*, 75, 183, doi: <https://doi.org/10.2138/rmg.2013.75.7>
- Dixon, J. E., Stolper, E. M., & Holloway, J. R. 1995, *JPet*, 36, 1607, doi: <https://doi.org/10.1093/oxfordjournals.petrology.a037267>
- Duan, Z., Möller, N., & Weare, J. H. 1992, *GeCoA*, 56, 2605, doi: [https://doi.org/10.1016/0016-7037\(92\)90347-L](https://doi.org/10.1016/0016-7037(92)90347-L)
- Elkins-Tanton, L. 2008, *E&PSL*, 271, 181, doi: <https://doi.org/10.1016/j.epsl.2008.03.062>
- Fei, H., & Katsura, T. 2020, *E&PSL*, 531, 115987, doi: <https://doi.org/10.1016/j.epsl.2019.115987>
- Frost, D. J., & Wood, B. J. 1997, *GeCoA*, 61, 3301, doi: [https://doi.org/10.1016/S0016-7037\(97\)00168-3](https://doi.org/10.1016/S0016-7037(97)00168-3)
- Gaillard, F., Bouhifd, M. A., Füü, E., et al. 2021, *SSRv*, 217, 22, doi: <https://doi.org/10.1007/s11214-021-00802-1>
- Gooding, J. L., & Muenow, D. W. 1977, *Metic*, 12, 401, doi: <https://doi.org/10.1111/j.1945-5100.1977.tb00458.x>
- Grewal, D. S., Dasgupta, R., & Farnell, A. 2020, *GeCoA*, 280, 281, doi: <https://doi.org/10.1016/j.gca.2020.04.023>
- Grimm, S. L., & Heng, K. 2015, *ApJ*, 808, 182, doi: <https://doi.org/10.1088/0004-637X/808/2/182>
- Grimm, S. L., Malik, M., Kitzmann, D., et al. 2021, *ApJS*, 253, 30, doi: <https://doi.org/10.3847/1538-4365/abd773>
- Gronoff, G., Arras, P., Baraka, S. M., et al. 2020, *JGRA*, 125, e2019JA027639, doi: <https://doi.org/10.1029/2019JA027639>
- Hamano, K., Abe, Y., & Genda, H. 2013, *Natur*, 497, 607, doi: <https://doi.org/10.1038/nature12163>
- Hamano, K., Kawahara, H., Abe, Y., Onishi, M., & Hashimoto, G. L. 2015, *ApJ*, 806, 216, doi: <https://doi.org/10.1088/0004-637X/806/2/216>
- Hamilton, D., & Oxtoby, S. 1986, *JG*, 94, 626
- Hier-Majumder, S., & Hirschmann, M. M. 2017, *GGG*, 18, doi: <https://doi.org/10.1002/2017GC006937>

- Hirschmann, M., Withers, A., Ardia, P., & Foley, N. 2012, *E&PSL*, 345–348, 38, doi: <https://doi.org/10.1016/j.epsl.2012.06.031>
- Hirschmann, M. M. 2012, *E&PSL*, 341–344, 48, doi: <https://doi.org/10.1016/j.epsl.2012.06.015>
- . 2016, *AmMin*, 101, 540, doi: <https://doi.org/10.2138/am-2016-5452>
- . 2018, *E&PSL*, doi: <https://doi.org/10.1016/j.epsl.2018.08.023>
- Holloway, J. R., & Blank, J. G. 1994, in *Volatiles in magmas*, ed. M. R. Carroll & J. R. Holloway, Vol. 30 (Mineralogical Society of America), 187–230, doi: <https://doi.org/10.1515/9781501509674-012>
- Iacono-Marziano, G., Morizet, Y., Trong, E. L., & Gaillard, F. 2012, *GeCoA*, 97, 1, doi: <https://doi.org/10.1016/j.gca.2012.08.035>
- Karman, T., Gordon, I. E., van der Avoird, A., et al. 2019, *Icarus*, 328, 160, doi: <https://doi.org/10.1016/j.icarus.2019.02.034>
- Katyal, N., Ortenzi, G., Grenfell, J. L., et al. 2020, *A&A*, 643, doi: <https://doi.org/10.1051/0004-6361/202038779>
- Keppler, H., & Golabek, G. 2019, *Geochemical Perspectives Letters*, 11, doi: <https://doi.org/10.7185/geochemlet.1918>
- Labrosse, S., Hernlund, J. W., & Coltice, N. 2007, *Natur*, 450, 866, doi: <https://doi.org/10.1038/nature06355>
- Lange, M. A., & Ahrens, T. J. 1982, *Icarus*, 51, 96, doi: [https://doi.org/10.1016/0019-1035\(82\)90031-8](https://doi.org/10.1016/0019-1035(82)90031-8)
- Lebrun, T., Massol, H., Chassefère, E., et al. 2013, *JGRE*, 118, 1155, doi: <https://doi.org/10.1002/jgre.20068>
- Lécuyer, C., Gillet, P., & Robert, F. 1998, *ChGeo*, 145, 249, doi: [https://doi.org/10.1016/S0009-2541\(97\)00146-0](https://doi.org/10.1016/S0009-2541(97)00146-0)
- Li, G., Gordon, I. E., Rothman, L. S., et al. 2015a, *ApJS*, 216, 15, doi: <https://doi.org/10.1088/0067-0049/216/1/15>
- Li, Y., Dasgupta, R., & Tsuno, K. 2015b, *E&PSL*, 415, 54, doi: <https://doi.org/10.1016/j.epsl.2015.01.017>
- Lichtenberg, T., Bower, D. J., Hammond, M., et al. 2021, *JGRE*, e2020JE006711, doi: <https://doi.org/10.1029/2020JE006711>
- Maas, C., & Hansen, U. 2019, *E&PSL*, 513, 81, doi: <https://doi.org/10.1016/j.epsl.2019.02.016>
- Marty, B. 2012, *E&PSL*, 313–314, 56, doi: <https://doi.org/10.1016/j.epsl.2011.10.040>
- Maurice, M., Tosi, N., Samuel, H., et al. 2017, *JGRE*, 122, 577, doi: <https://doi.org/10.1002/2016JE005250>
- McKenzie, D. 1984, *JPet*, 25, 713, doi: <https://doi.org/10.1093/petrology/25.3.713>
- McMillan, P. F. 1994, in *Volatiles in Magmas*, ed. M. R. Carroll & J. R. Holloway, Vol. 30 (Mineralogical Society of America), 131–156, doi: <https://doi.org/10.1515/9781501509674-010>
- Miyazaki, Y., & Korenaga, J. 2021, *Astrobiology*, <https://arxiv.org/abs/2108.03759>
- Mosenfelder, J. L., Asimow, P. D., Frost, D. J., Rubie, D. C., & Ahrens, T. J. 2009, *JGRB*, 114, doi: <https://doi.org/10.1029/2008JB005900>
- Newcombe, M., Brett, A., Beckett, J., et al. 2017, *GeCoA*, 200, 330, doi: <https://doi.org/10.1016/j.gca.2016.12.026>
- Nikolaou, A., Katyal, N., Tosi, N., et al. 2019, *ApJ*, 875, 11, doi: <https://doi.org/10.3847/1538-4357/ab08ed>
- Olson, P. L., & Sharp, Z. D. 2019, *PEPI*, 294, 106294, doi: <https://doi.org/10.1016/j.pepi.2019.106294>
- O’Neill, H. S., & Eggins, S. M. 2002, *ChGeo*, 186, 151, doi: [https://doi.org/10.1016/S0009-2541\(01\)00414-4](https://doi.org/10.1016/S0009-2541(01)00414-4)
- Pan, V., Holloway, J. R., & Hervig, R. L. 1991, *GeCoA*, 55, 1587, doi: [https://doi.org/10.1016/0016-7037\(91\)90130-W](https://doi.org/10.1016/0016-7037(91)90130-W)
- Patočka, V., Calzavarini, E., & Tosi, N. 2020, *PhRvF*, 5, doi: <https://doi.org/10.1103/PhysRevFluids.5.114304>
- Perera, V., Jackson, A. P., Elkins-Tanton, L. T., & Asphaug, E. 2018, *JGRP*, 123, 1168, doi: <https://doi.org/10.1029/2017JE005512>
- Putirka, K. D., & Rarick, J. C. 2019, *AmMin*, 104, 817, doi: <https://doi.org/10.2138/am-2019-6787>
- Raymond, S. N., & Izidoro, A. 2017, *Icarus*, 297, 134, doi: <https://doi.org/10.1016/j.icarus.2017.06.030>
- Raymond, S. N., Quinn, T., & Lunine, J. I. 2007, *AsBio*, 7, 66, doi: <https://doi.org/10.1089/ast.2006.06-0126>
- Rothman, L. S., Gordon, I. E., Barber, R. J., et al. 2010, *JQSRT*, 111, 2139, doi: <https://doi.org/10.1016/j.jqsrt.2010.05.001>
- Rubie, D., Nimmo, F., & Melosh, H. 2015, in *Treatise on Geophysics*, 2nd edn., ed. G. Schubert, Vol. 9 (Elsevier), 43–79, doi: <https://doi.org/10.1016/B978-0-444-53802-4.00154-8>
- Rumpf, H. C. H., & Gupte, A. R. 1971, *Chemie Ingenieur Technik*, 43, 367, doi: <https://doi.org/10.1002/cite.330430610>
- Salvador, A., Massol, H., Davaille, A., et al. 2017, *JGRE*, 122, 1458, doi: <https://doi.org/10.1002/2017JE005286>
- Scaillet, B., & Gaillard, F. 2011, *Natur*, 480, 48, doi: <https://doi.org/10.1038/480048a>
- Schaefer, L., & Fegley, B. 2010, *Icarus*, 208, 438, doi: <https://doi.org/10.1016/j.icarus.2010.01.026>
- . 2017, *ApJ*, 843, 120, doi: <https://doi.org/10.3847/1538-4357/aa784f>

- Schaefer, L., Wordsworth, R. D., Berta-Thompson, Z., & Sasselov, D. 2016, *ApJ*, 829, 63, doi: <https://doi.org/10.3847/0004-637X/829/2/63>
- Solomatov, V. S., Olson, P., & Stevenson, D. J. 1993, *E&PSL*, 120, 387, doi: [https://doi.org/10.1016/0012-821X\(93\)90252-5](https://doi.org/10.1016/0012-821X(93)90252-5)
- Solomatov, V. S., & Stevenson, D. J. 1993a, *JGRE*, 98, 5375, doi: <https://doi.org/10.1029/92JE02948>
- . 1993b, *JGRE*, 98, 5391, doi: <https://doi.org/10.1029/92JE02579>
- Sossi, P. A. 2021, *NatAs*, doi: <https://doi.org/10.1038/s41550-021-01353-9>
- Sossi, P. A., Burnham, A. D., Badro, J., et al. 2020, *SciA*, 6, doi: <https://doi.org/10.1126/sciadv.abd1387>
- Sossi, P. A., Tollan, P., Badro, J., & Bower, D. J. 2021, *E&PSL*
- Stolper, E. 1982, *GeCoA*, 46, 2609, doi: [https://doi.org/10.1016/0016-7037\(82\)90381-7](https://doi.org/10.1016/0016-7037(82)90381-7)
- Stolper, E., & Holloway, J. R. 1988, *E&PSL*, 87, 397, doi: [https://doi.org/10.1016/0012-821X\(88\)90004-0](https://doi.org/10.1016/0012-821X(88)90004-0)
- Tagawa, S., Sakamoto, N., Hirose, K., et al. 2021, *NatCo*, 12, 2588, doi: <https://doi.org/10.1038/s41467-021-22035-0>
- Takahashi, S., Ohtani, E., Terasaki, H., et al. 2013, *PCM*, 40, 647, doi: <https://doi.org/10.1007/s00269-013-0600-x>
- Thompson, M. A., Telus, M., Schaefer, L., et al. 2021, *NatAs*, doi: <https://doi.org/10.1038/s41550-021-01338-8>
- Tonks, W., & Melosh, H. 1990, in *Origin of the Earth*, ed. H. E. Newsom & J. H. Jones (Oxford University Press, New York), 151–174
- Tu, L., Johnstone, C. P., Güdel, M., & Lammer, H. 2015, *A&A*, 577, L3, doi: <https://doi.org/10.1051/0004-6361/201526146>
- Wilson, L., & Head III, J. W. 1981, *JGRB*, 86, 2971, doi: <https://doi.org/10.1029/JB086iB04p02971>
- Wolf, A. S., & Bower, D. J. 2018, *PEPI*, 278, 59, doi: <https://doi.org/10.1016/j.pepi.2018.02.004>
- Yoshioka, T., Nakashima, D., Nakamura, T., Shcheka, S., & Keppler, H. 2019, *GeCoA*, 259, 129, doi: <https://doi.org/10.1016/j.gca.2019.06.007>
- Yurchenko, S. N., & Tennyson, J. 2014, *MNRAS*, 440, 1649, doi: <https://doi.org/10.1093/mnras/stu326>
- Yurchenko, S. N., Tennyson, J., Barber, R. J., & Thiel, W. 2013, *JMoSp*, 291, 69, doi: <https://doi.org/10.1016/j.jms.2013.05.014>
- Zahnle, K. J., Gacesa, M., & Catling, D. C. 2019, *GeCoA*, 244, 56, doi: <https://doi.org/10.1016/j.gca.2018.09.017>
- Zahnle, K. J., Lupu, R., Catling, D. C., & Wogan, N. 2020, *PSJ*, 1, 11, doi: <https://doi.org/10.3847/psj/ab7e2c>